The effect of vessel holes on fracture behaviour in the femoral neck of the human femur

Karin Odin & Sofia Rokkones

Lund, June 2020

Master's Thesis in Biomedical Engineering

Faculty of Engineering, LTH
Department of Biomedical Engineering

Supervisors: Lorenzo Grassi, Joeri Kok, and Hanna Isaksson

Title

The effect of vessel holes on fracture behaviour in the femoral neck of the human femur

Author

Karin Odin & Sofia Rokkones

Figures

Created by the authors if nothing else is indicated

Acknowledgements

We would first of all like to thank our supervisors, Lorenzo Grassi, Joeri Kok, and Hanna Isaksson. Thank you for all your encouragement and guidance throughout this project. It has been an educative time and we have learned a lot that we can bring with us in life. Also, thank you for your fantastic communication and presence, especially during the second half of the master thesis, executed during a worldwide pandemic, working from home due to social distancing constraints. Thank you also to all the members of the Biomechanic group, making us feel very welcome as a part of the team already from day one.

Abstract

Hip fractures are widely spread in today's society and affect a person's quality of life. Osteoporosis is a bone disease that results in more fragile bones and an increased risk of bone fractures, including hip fractures. A method proposed for assessing the fracture risk is finite element (FE) models of the femur. These FE models proved to be effective in predicting the overall mechanical behavior of human femurs, but are less accurate in predicting localization of stresses or strains. It is proposed that vessel holes in the femoral neck may affect the ability of FE models to predict fracture location, and that they need to be accounted for.

There were two main aims for this thesis. The first, was to develop an automatic method for detection and quantification of blood vessel holes present in the proximal human femur. The second, was to investigate whether a micro-FE model, based on micro-CT images including features such as vessel holes, could more effectively identify local high strains as compared to an FE model based on lower resolution clinical CT images.

Investigating these issues, the project focused on image analysis developing a method with which blood vessel holes could be quantified in a feasible and accurate way in both micro-CT and clinical CT images. This was done by investigating vessel hole canal structures and by thickness calculation of the cortical bone. The project also focused on developing and validating a finite element model of the femur bone, based on segmentation and mesh generation from micro-CT images.

The project resulted in proposed methods for detecting and quantifying vessel holes, both based on micro-CT and clinical CT images. The methods were automatic, and the results showed a 100% accuracy in the micro-CT, and 60% accuracy in the clinical CT compared to the micro-CT. Furthermore, a micro-FE model, with a complex surface structure including the detected vessel holes, was developed showing higher accuracy in strain prediction, compared to an FE model based

on clinical CT images.

The conclusion was that vessel holes could be detected and quantified fully from micro-CT images and the largest vessel holes also in clinical CT images. Also, a micro-FE model generated based on micro-CT images, including the vessel holes in the femoral neck, correlated better than a similar model based on clinical CT images to experimentally measured strains.

List of acronyms & abbreviations

ε - strain

ρ_{app} - apparent density

ρ_{ash} - ash density

σ - stress

BC - boundary condition

BMD - bone mineral density

CT - computed tomography

DIC - digital image correlation

E - young's modulus

FE - finite element

FEA - finite element analyses

PDE - partial differential equation

PVE - partial volume effect

ROI - region of interest

SD - standard deviation

Contents

Chapter 1

Introduction

In today's society, a large group of people are affected by osteoporosis, a bone disease reducing the bone mineral density, leading to more fragile bones and a higher risk of fracture. Today, one in three women and one in five men older than 50 years will sustain an osteoporosis-related fracture within their lifetime [1]. In the year 2017, the number of fragility fractures was 120 000 in Sweden. This corresponds to more than 13 fractures every hour, and is estimated to increase in the coming years [2].

Hip fractures account for about 20% of all osteoporotic fractures worldwide. Nevertheless, they account for the majority of the osteoporotic fracture-related costs among men and women over 50 years [3]. In Sweden alone, the cost of hip fractures was €823 million in 2010 [4]. Worldwide, the prevalence of hip fractures is predicted to increase from 1.3 million in the year 1990 to between 7.3 - 21.3 million in 2050 [5].

The most common way of diagnosing osteoporosis is to measure the bone mineral density (BMD), to get a so-called T-score. If the BMD value is 2.5 standard deviations (SDs) or more below the average BMD value for premenopausal women, the patient is considered osteoporotic [6, 7, 8]. A low BMD is connected to high fracture risk. However, a majority of the hip fractures occur in people without osteoporosis [9].

A proposed method for improved assessment of the fracture risk is by using finite element (FE) models of the femur (thigh bone), based on patient specific information, geometry and mechanical properties derived from computed tomography (CT) images. Finite element analysis (FEA) can estimate the strength and fracture risk of the femur [10].

Several approaches to determine the fracture risk in the femur with FE models have been developed over the last decades. Yet, there is a

need for more detailed models. Recent studies have detected regions of local weaknesses in the femoral neck which correspond to regions where blood vessel holes are located in the cortical bone [11]. It is suggested that the vessel holes, which are not accounted for in today's FE models, may be involved in fracture initiation in the femoral neck [11, 12]. Experimental results have been compared to predicted outcomes from FE models of femurs under load. The results correspond well in all regions, except in the superolateral region, the "saddle-region" of the femoral neck. Here, the FE models predicted high strains that were never detected experimentally. Instead, the experimental results showed high strains in several vessel holes, which the FE models did not predict. To improve the accuracy of future FE models' ability to predict the femur's risk of fracture, the vessel holes are proposed to be accounted for [13, 14].

1.1   Aim

The purpose of the thesis was to determine the presence and location of blood vessel holes in the femoral neck and to investigate their effect on the local strain distribution. This was done by developing different approaches to quantify the vessel holes in the femoral neck and to build FE models that included the characteristics of the vessel holes. The main objectives were divided into two sub-aims, namely:

- To develop an automatic method for detection and quantification of blood vessel holes, in terms of size and location, in both micro-CT and clinical CT images.

- To investigate whether a micro-FE model based on micro-CT images, including features such as vessel holes, can more effectively identify local high strains as compared to an FE model based on lower resolution clinical CT images.

1.2   Design of the study

The starting point for this master's thesis was that clinical CT images and FE models based on these clinical CT images were available. Experimental measurements have shown that strains locally are high in the region of the femoral neck where a large number of blood vessel holes

usually are present. In order to investigate how the vessel holes influence the bone strength and possibly affect the fracture risk of the femur, two approaches were used. First, a method was proposed for detecting and quantifying the number, size, and location of vessel holes present in the femoral neck, both using high resolution micro-CT and clinical CT images. Secondly, based on micro-CT images of high resolution, a way of generating micro-FE models was developed. By introducing vessel holes in the model, they can hopefully, detect local high strains at the femoral neck in a more accurate way.

1.3 Authors' contribution

The thesis consists of two main parts, the image analysis and the FE modeling. Sofia Rokkones has focused on the image analysis part, performing detection and quantification of the vessel holes in the femoral neck. Also, segmentation and generation of 3D meshes of the femur have been a responsibility. The FE modeling and analysis have been done by Karin Odin, focusing on FE modeling based on both clinical CT and micro-CT images. The two focus areas in the project made the work more efficient and at the same time enabled close collaboration and discussion between the authors, which facilitated the progress. The two authors have contributed equally to the writing of the report.

Chapter 2

Background

This chapter contains the background and theory required for this thesis. It includes the human femur, insights in its anatomy, and fracture risks and risk assessments as motivation for numerical analysis and modelling. The chapter is also presenting theory regarding techniques used and implemented along the project.

2.1   Anatomy

2.1.1   Anatomical directions

The anatomical directions are the terms of how the human anatomy is referred to, and can be seen in Figure 2.1. The terms most frequently used in this thesis are superior, proximal, lateral and posterior.

2.1.2   Femur

Anatomy of the femur

The femur is the longest bone in the human body and the most proximal part of the human leg, connecting the pelvis with the knee (Figure 2.2). The proximal part of the femur consists of a head, neck and shaft, as can be seen in Figure 2.2, and is the main focus in this project. The neck connects the head with the shaft, and on the lateral side of the neck, the greater trochanter is located. Continuing distally, the lesser trochanter is positioned on the posterior side of the proximal part of the shaft. Femur, as a part of the hip joint, is important to enable locomotion when walking, running, going up steps, and sitting [16].
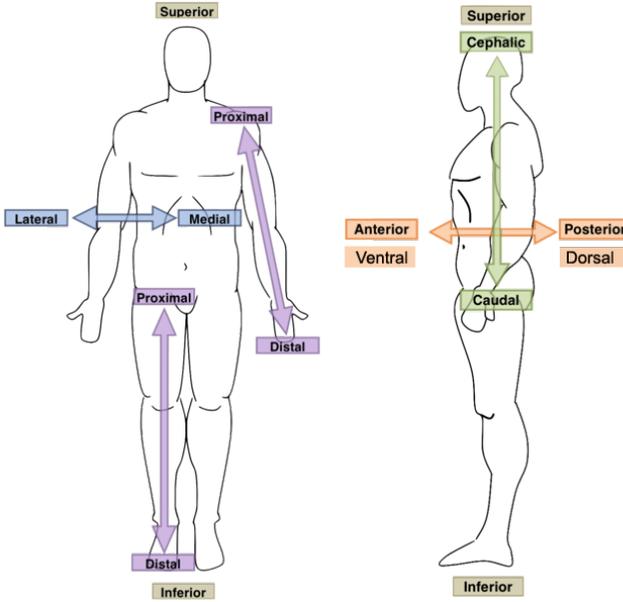
Figure 2.1: Anatomical applied directions on the human body [15].
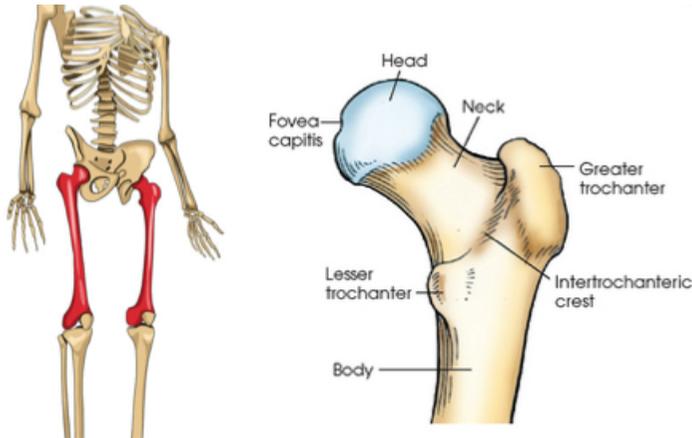
Figure 2.2: Left - femur position in the body [17]. Right - posterior view of the proximal femur's anatomy [18].

Composition of the bone

The outer surface of the femur consists of hard cortical bone, and the inside is composed of trabecular bone, a porous structure, as can be seen in Figure 2.3. The two different structures in the bone are of great importance since this gives rise to highly different mechanical

properties of cortical and trabecular bone [19]. The exterior cortical bone is compact and have a high stiffness. The trabecular bone is a weaker structure where bone tissue is arranged in a network also containing blood vessels and marrow [19].
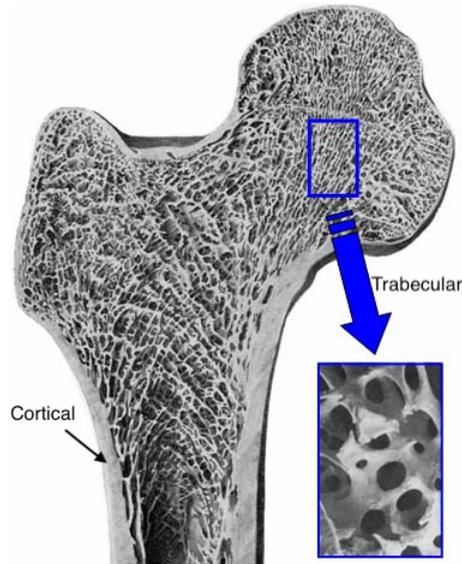
Figure 2.3: The surface of the femur consists of a hard, cortical layer while the inner part is built up as a porous structure [20].

Vascular supply and vessel holes

The femoral head and neck junction are supplied with nutrients by blood vessels perforating the cortical bone. The total amount of vascular holes in the region varies between individuals, and can range from 8 to 21 [21]. Approximately 80% of the vessel holes, are located at the superior side of the femoral neck [22]. Of those holes, more than 50% are smaller than 1 mm in diameter and less than 24% are larger than 2 mm in diameter. Earlier studies have concluded that clinical CT imaging is unable to estimate the number of vessel holes due to too low resolution [21].

2.2 Osteoporosis

Osteoporosis is a bone disease defined as reduced bone density and quality. This leads to porous and more fragile bones, which increases the

risk of fracture. The disease is more prevalent in the older population, and especially in older women [1].

As many as 46% of the women, and 29% of the men in Sweden above the age of 50 years, will sustain a fracture caused by osteoporosis in their remaining lifetime. Sweden is, comparing to six other countries in the EU, the country where the people have the highest risk for fragility fractures [2] (Figure 2.4a). The lifetime risk for a hip fracture specifically, for men and women over 50 years, is also highest in Sweden among the same six countries (Figure 2.4a). The hip fractures stand for 20% of the fragility fractures, but 57% of the total costs (Figure 2.4b). In 2017, the total cost of fragility fractures in the six countries investigated (according Figure 2.4a) was estimated to €37.5 billion, and is expected to increase with 27% until 2030 [2].

(a) Lifetime risk of fragility fractures, compared with CVD.

(b) Distribution of fracture type and costs.
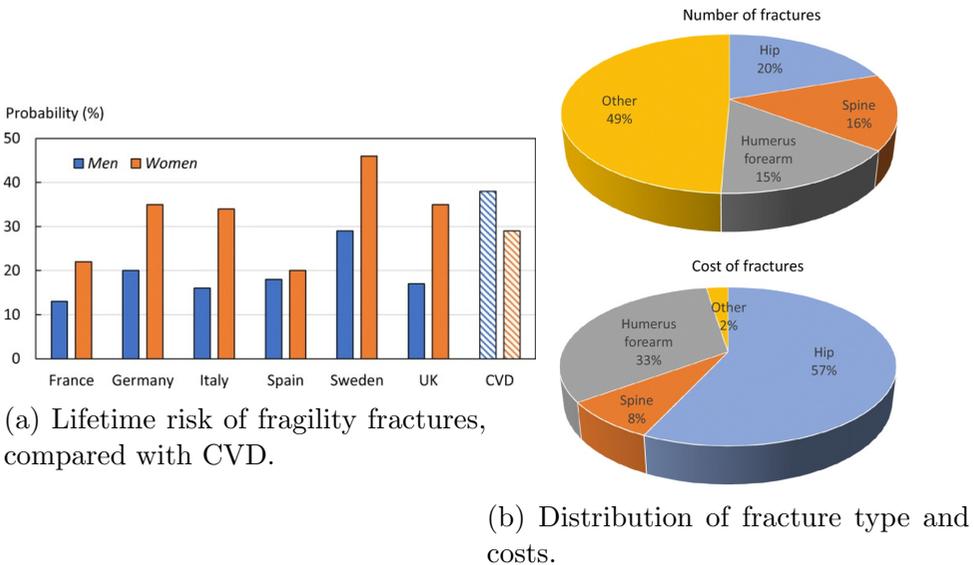
Figure 2.4: (a) the lifetime risk of fragility fractures after the age of 50 years, compared with the equivalent risk for cardiovascular disease (CVD) in Europe, is presented. (b) the occurrence versus the cost of different fracture types are presented [2].

In addition to the large fracture risk among the people and the high costs, a hip fracture also causes a lot of pain and reduced quality of life for the individual [2].

2.3 CT imaging

In this project, both images from clinical computed tomography (CT) and micro-CT were used. The two techniques are similar in principle, but, implemented differently and have different application areas.

Clinical CT scanning is an imaging technique based on X-ray, where an object is exposed to X-rays from multiple angles. On the opposite side of the object, the X-rays are detected by X-rays detectors. The object absorbs an amount of radiation and the total absorption depends on various factors, such as the object's size and density. Each rotation evolves in a 2D slice of the object, a projection image. When the CT has imaged every 2D slice of the object, the slices are reconstructed, and showed as a 3D object digitally. Every slice represents a thickness of 1-10 millimeters of the object, depending on the CT machine [23]. This technique is primarily used clinically.

Micro-CT is imaging on a smaller scale, with a higher resolution. From 1 millimeter resolution in the clinical CT to 1 micron, a thousand of a millimeter and smaller in the micro-CT. In micro-CT imaging, the CT scanner is typically still and the object is rotating. The application areas for micro-CT are for example material science, small animals, and ex-vivo imaging of human tissues [24].

The reconstruction of a CT image can be done with different settings, where, among others, the convolution kernel is one. The kernel is a weighting factor, filtering the CT image. There are two main processes, high-pass filtering and low-pass filtering, reconstructing the image into a sharpened, edge enhanced, image, respectively a smoothed, blurred image [25]. These kernels are referred to as 'hard' and 'smooth', respectively.

2.4 Digital image correlation

Digital image correlation (DIC) is a non-contact optical technique used for measuring strains and displacements during experimental testing [26]. DIC is based on digital image processing and numerical computing. The basic principle of the method is to trace physical points from a reference configuration to a deformed configuration (Figure 2.5) [27].

To prepare a sample for DIC measurement, the component investigated is covered with a randomized pattern, for example, black dots speckled on a white surface. By tracking blocks of pixels with cam-
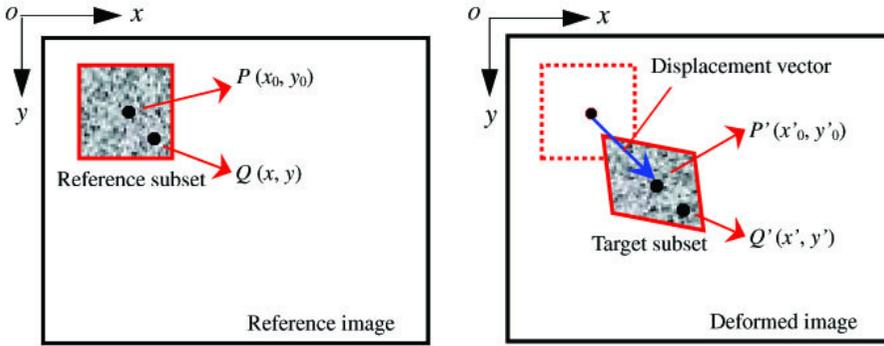
Figure 2.5: The principle of DIC [27]. A block of pixels is traced with cameras from a reference to a deformed image, resulting in full-field measurements of the displacement over a surface.

eras, the displacements at the surface can be measured, resulting in a full-field measurement of the displacements, and enabling calculations of full-field strain data. DIC can be performed both in 2D and 3D depending on the setup. Using one camera, the full-field strains for a flat (2D) surface, and using two cameras the full-field displacements for a 3D surface, can be generated [28].

2.4.1   Interpretation of DIC measurements

The DIC measurements can be used as a comparison to strains predicted by FE models. One way of comparing strains measured by DIC and predicted by FE models is by correlation analysis. The basic idea is to compare two measurements, resulting in a correlation coefficient (R), ranging from -1.0 to +1.0. The closer R is to either end of this range, the stronger the linear relationship between the two are [29]. Commonly used is also the correlation of determination (R^2), indicating the amount of variance introduced in the model. In general, a high value of R^2 is an indication that the model is a good fit for the data [30]. Another way of investigating correlation was proposed by Martin Bland and Douglas Altman, named Bland-Altman analysis [29]. Bland-Altman analysis determines the difference between measurements with a graphical method, representing the measurements with a scatterplot where the x-axis represents the average and the y-axis represents the difference of two measurements (Figure 2.6). A Bland-Altman plot usually also includes the 95% confidence interval as marked with red lines

in the figure. A strong correlation is indicated by a small difference between measurements (the mean is close to zero), that the distribution of differences is equally spread around the mean and that confidence interval is narrow.
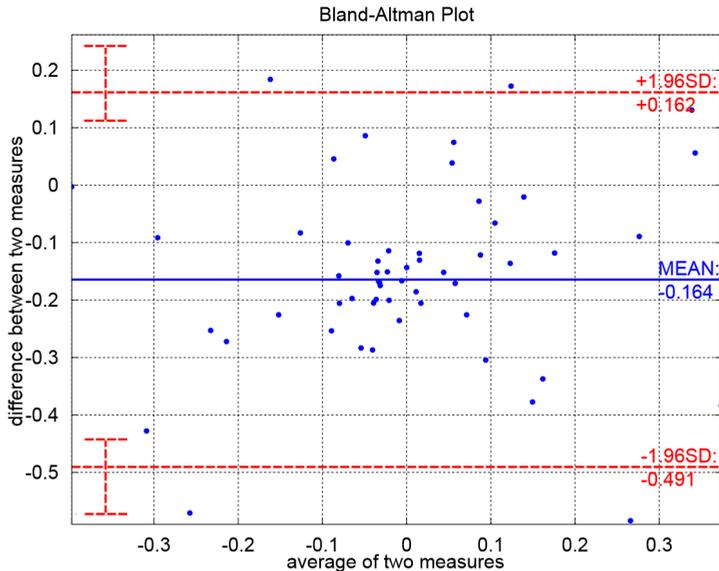
Figure 2.6: Example of a Bland-Altman plot used for correlation of two measures. The x-axis represents the average and the y-axis represents the difference of two measurements [31]

.

2.5 Image segmentation

2.5.1 Threshold segmentation

Threshold segmentation is a digital image processing method, which can be used to create binary images by replacing every pixel with intensity less than a selected constant (a threshold) to a black pixel, or to a white pixel if the pixel has a greater intensity value than the constant. Thresholding is a powerful and simple technique for image segmentation and can be applied both globally and locally. The selection of the threshold can be based on, for example, visual assessment, the histogram of tonal distribution, optimization, or spatial information [32]. In this project,

the threshold is often applied as a single threshold, and determined from the histogram shape and by visually examining the image.

2.5.2 Active contour segmentation

Active contour segmentation is developed to segment anatomical structures [33]. The method used in this project is based on the 3D contour segmentation method *Geodesic Active Contours* [34, 35]. The technique is a semiautomatic active contour evolution method, where the final segmentation is represented by contours, the edge structure of the segmentation. A closed surface represents an evolving contour - edges of the closed surface grow, which makes its volume increase. The surface is growing with regard to internal and external forces, speeding up or slowing down the growth rate, and determining where it is allowed to grow. The surface grows according to a partial differential equation (PDE), simplified as:

$$C_t = (\alpha g_I - \beta \kappa)\vec{n} \tag{2.1}$$

where α can be described as the region competition force and β as the smoothing (curvature) force. C_t is the contour evolving in time step t, g_I is the speed function, κ) is the mean curvature of the contour, and $\vec{n}$ is the unit normal to the contour. By setting α and β to 1, the method *Geodesic Active Contours* is obtained.

The 3D active contour segmentation is performed stepwise. Firstly, a speed map, or probability map, is created by threshold segmentation of the image. The contour is not allowed to evolve outside of the segmented region. Secondly, the segmentation is initialized by seeds placed in areas to segment. At last, parameters in the active contour evolution PDE are set, determining internal, external, and smoothing forces. The segmentation evolves for an optional amount of iterations, controlled by the user [33].

2.6 Calculation of cortical bone thickness

Cortical bone thickness calculation can be performed in Stradview (Version 6.05, Medical Research Imaging Group, Cambridge University, Engineering Department) [36]. One technique for calculation of cortical bone thickness is called *Cortical Bone Mapping (CBM)* [37]. By fitting a piecewise constant function along the surface normal, the cortical thickness is estimated by the CT image's density variation in intensity

along the line [38] (Figure 2.7). The cortical bone's outer and inner surfaces are calculated, and by that the thickness. The technique, and the line width and length are settings possible to choose for the user.
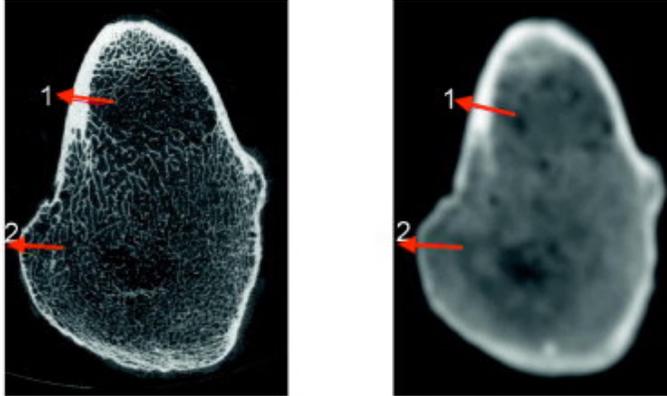
(a) Left - high resolution CT. Right - low resolution CT.
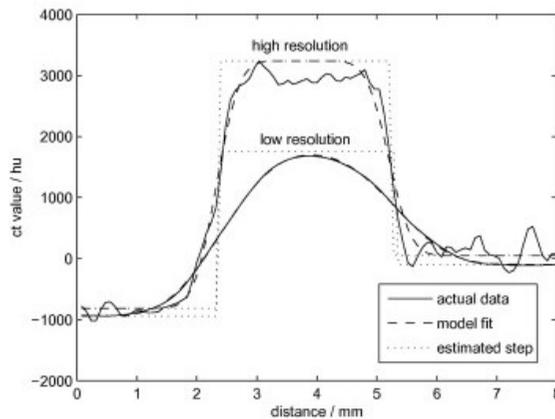
(b) Line 1 - thickness estimate.

Figure 2.7: An example of cortical bone thickness calculation. (a) the CT images with two red arrows representing the line along the surface normal of where the function estimates the cortical thickness. (b) intensity profile of the image along arrow 1 with the calculated thickness based on its profiles [38].

2.7 Finite element bone models

Two important measures for fracture estimation are stress (σ) and strain (ε). Previous studies have suggested that the fracture initiation of bone is strain-driven [39]. For this reason it is of great interest to study the strains detected in the femur during a fall. Furthermore, it has been shown that the yield strain depends on anatomical site [40] and, during a side-ways fall, compressive strains dominate at the superolateral femoral neck [14]. These observations are the basis of studying the compressive strains located in the femoral neck.

The strains in this project can be described by the simplified principal strain matrix, Equation 2.2,

$$\varepsilon = \begin{bmatrix} \varepsilon_1 & 0 & 0 \\ 0 & \varepsilon_2 & 0 \\ 0 & 0 & \varepsilon_3 \end{bmatrix} \tag{2.2}$$

where ε_1 is the major principal strain and ε_3 is the minor principal strain. In most situations, the major principal strain is a measure of the tensile strains and the minor principal strain a measure of the compressive strains. Since the femoral neck mainly experiences compressive strains, the minor principal strains are a good way of measuring the magnitude of strains at the femoral neck.

2.7.1 The finite element method

The FE method is a numerical solution algorithm with which differential equations can be solved approximately. The basic idea is to first divide the region where a certain differential equation holds into many small parts, or finite elements [41]. Instead of finding approximations that would hold for the entire region, approximations are made for each element and the total behavior is determined by assembling the response in all finite elements. An assembly of finite elements is called a mesh.

In simplified words, an FE model is a mesh based on finite elements together with additional information regarding the material properties of the elements, the coordinate system by which the model is oriented and possible restrictions regarding the degrees of freedom. In this thesis, the term micro-FE model is frequently being used. What is being referred to by this is a FE model based on high resolution micro-CT images.

2.7.2 Mesh representations

In the thesis, two types of mesh representations are being used, surface meshes and volume meshes. A surface mesh consists of triangular elements where every element consists of three connected nodes. The nodes can be located anywhere in space and the complete surface mesh is a representation of the surface structure of a component, e.g. the femur. The internal structure of the femur is described using a volume mesh. There are many types of elements that can be used, but in this thesis, volume elements are exclusively tetrahedrons. Both four-node and ten-node tetrahedral elements were used (Figure 2.8).

(a) Four-node tetrahedral element   (b) Ten-node tetrahedral element
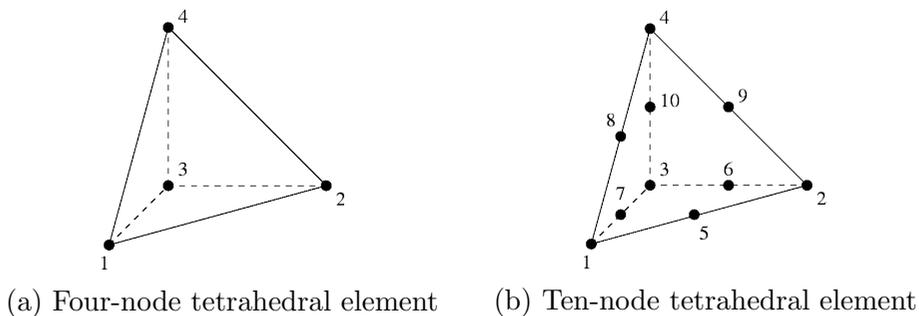
Figure 2.8: Tetrahedral elements are the building blocks for the volume mesh [42].

The reason for using the more complex ten-node, quadratic, elements is because in this way more integration points are introduced to a model which generally increases accuracy of the calculations, but at the same time increases the computational cost.

2.7.3 Mapping material properties to the FE model

As mentioned earlier, the bone consists of cortical and trabecular bone with differences in strength and composition. This is included in the FE model by mapping a stiffness as a value for Young's modulus onto each tetrahedral element in the volume mesh.

Calibration of CT images

In order to map a correct value for the Young's modulus onto elements, a calibration between CT grey values and bone mineral density is performed. This require that CT images of the specimen was taken together

with a number of phantoms with known density of mineral bone equivalent material. For each phantom, the grey value is measured and by making a plot of the grey value vs. the density and making a linear regression, you get a linear relation describing how the bone mineral density depend on the average grey value.

Bonemat

The mapping can be performed using the software Bonemat [43], and for this project an in-house Matlab implementation of Bonemat was used, mapping each element to the corresponding coordinates of a CT image. The average grey value of the CT image within a element is determined and by calibrating the grey-values to bone mineral density, each element is assigned a value for the average bone density inside, which somewhat correspond to the ash density (ρ_{ash}).

There are two common ways of describing bone mineral density, ash density and apparent density (ρ_{app}). The relation between the two types of density is described in Equation 2.3 [44].

$$\rho_{ash}/\rho_{app} = 0.6 \qquad (2.3)$$

Using this relation, the density of an element can then be transformed to Young's modulus (E) in MPa according to Equation 2.4 [45].

$$E = 6850 \cdot \rho_{app}^{1.49} \qquad (2.4)$$

Partial Volume Effect

Partial volume effects (PVE) is an important concept influencing the quality of the material mapping. For the reason that the average grey value within each element is determined, elements could get mapped with a lower density than the true density. For example, if an element is larger than the thickness of the cortical bone, the value for the mapped density could be significantly lower than the density of the cortical bone which affects the stiffness at the surface. This behaviour needs to be considered, both in the modelling, and in the validation procedure.

2.8 Background research for this project

It has been shown that FE models of the human femur based on clinical CT images can predict deformations with very high accuracy when compared to DIC measurements, and are able to predict the femoral strength with an error below 2% [28]. The FE models are based on clinical CT images, and are also taking the bone mineral density (BMD) into account. This makes it possible to include mechanical characteristics of the bone, and obtain accurate FE models that can be used for predicting a patient's fracture risk during screening [28].

Recent studies have detected regions of local weakness in the femoral neck which correspond to regions where vessel holes are perforating the cortical bone [11]. It is suggested that the vessel holes may be involved in the failure initiation in the femoral neck [11, 12].

When experimental measurements of strain have been compared to strains predicted by FE analyses of femurs in side-ways fall, they correlate well in all regions except the superior region in the femoral neck. High strains at the lateral superior region were predicted by the FE models, but not detected experimentally with DIC. Instead, high strains were measured experimentally in areas where vessel holes were present in the cortical bone. Those vessel holes are not represented by the FE models. It has been suggested that these vessel holes should be accounted for to get more accurate FE model predictions [13, 14].

Chapter 3

Materials & methods

3.1 Material

Micro-CT images (Figure 3.1) and clinical CT images (Figure 3.2) of one human femur were used in this project. The femur is one from a larger collection of fresh-frozen cadaver femurs, approved for use by The Finnish National Authority for Medicolegal Affairs (TEO, 5783/04/044/07). The femur had earlier been imaged with a clinical CT scanner (Siemens Somatom AS, pixel size 0.4-0.5mm, slice separation 0.6 mm, tube voltage 120 kV, tube current 210 mAs) and with a high-resolution laboratory x-ray tomographic device (Nikon XT H225, isotropic voxel size 52-60 μm, 100 kVp, 200 mAs). The femur came from the right side of a female donor, 81 years old, 160 cm, and 67 kg. [14]. The clinical scan was reconstructed with two different kernels, a smooth and a hard kernel.

3.2 Overview of the methods

This master's thesis can be divided into two main parts. The first part was more focused on image analysis, and to detect and quantify blood vessel holes from both micro-CT and clinical CT images. The second part of the project was more focused on computational modeling, and was to first generate a micro-FE model of the human femur and then to validate it using previously developed FE models. This sections gives a short description of the overview, and each section will be described in more detail later.
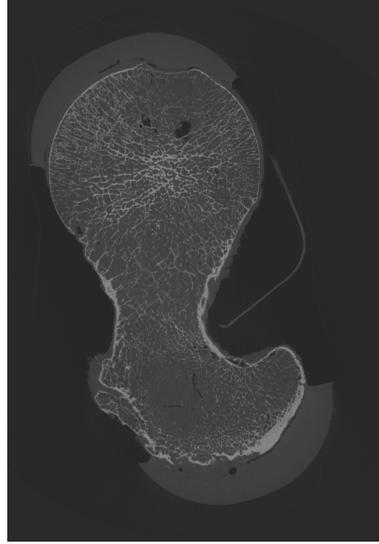
Figure 3.1: One slice of the micro-CT scan of the femur.
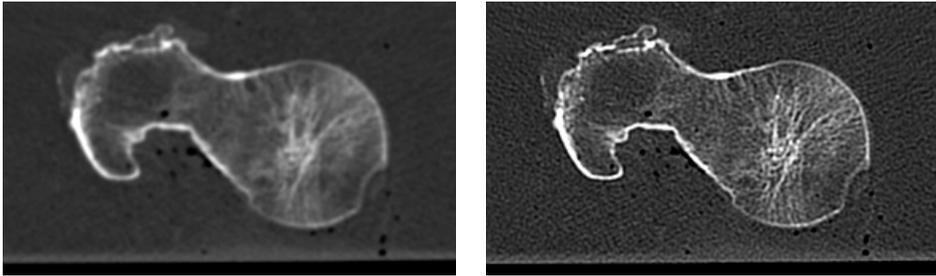
(a) Smooth kernel. (b) Hard kernel.

Figure 3.2: Clinical CT scans of the human femur reconstructed with a smooth (left), and a hard (rigth) kernel.

Quantification of vessel holes in micro- and clinical CT

Part of the project aimed to quantify vessel holes, in terms of their size and location, in the femoral neck. The conceptual method is shown in the flowchart in Figure 3.3. The quantification of vessel holes was separated into two different approaches, one for the micro-CT and one for the clinical CT. The micro-CT based approach started with a selection of the region of interest (ROI) in the femoral neck, from the micro-CT image. The ROI was segmented to extract the femur surface in detail, and a 3D geometry was obtained. The next step was to create a surface mesh of the femur. A downscaled micro-CT image was used, to segment

the outer surface of the femur. A mesh of the femur surface was obtained. The 3D geometry of ROI and the femur surface mesh were then used as input in a newly developed method for the detection and quantification of vessel holes. By fitting circles to the data, quantification data of vessel holes could be obtained. The clinical CT scan followed another approach, where the femur surface first was segmented and a surface mesh was generated. Based on the surface mesh, the cortical bone thickness was calculated in the femur. By detecting non-existing, or very low thickness in the cortical bone, vessel holes were detected in the femoral neck and quantified. The vessel holes' data from both approaches were then evaluated and compared.
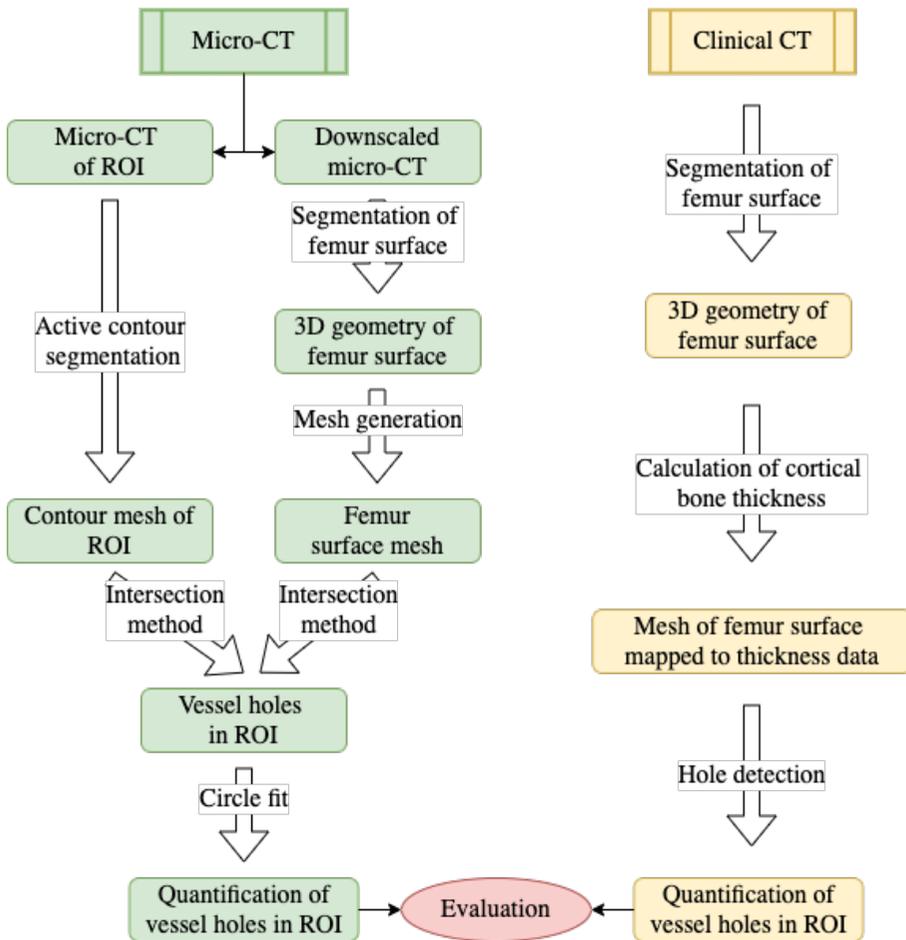

Figure 3.3: Flowchart over the quantification of vessel holes in micro- and clinical CT images.

Generation of FE models

FE-models based on clinical CT images have previously been developed within our research group [10]. These were used for validation of the models created during this project and will be referred to as the reference model. An overview of the steps in the generation of FE models can be found in the flowchart in Figure 3.4. A micro-FE model was created by segmentation of micro-CT images resulting in a surface mesh with high mesh density. By creating a volume mesh, mapping mechanical properties onto the finite elements and defining load and boundary conditions, a micro-FE model was created. For comparison and validation, a third FE model was created that will be referred to as the standard FE model. This model was segmented from clinical CT images and the surface mesh has a similar mesh as the reference model. A volume mesh was generated and mechanical properties, load and boundary conditions were set in the same way as for the micro-FE model. Calculated strains were compared between models.
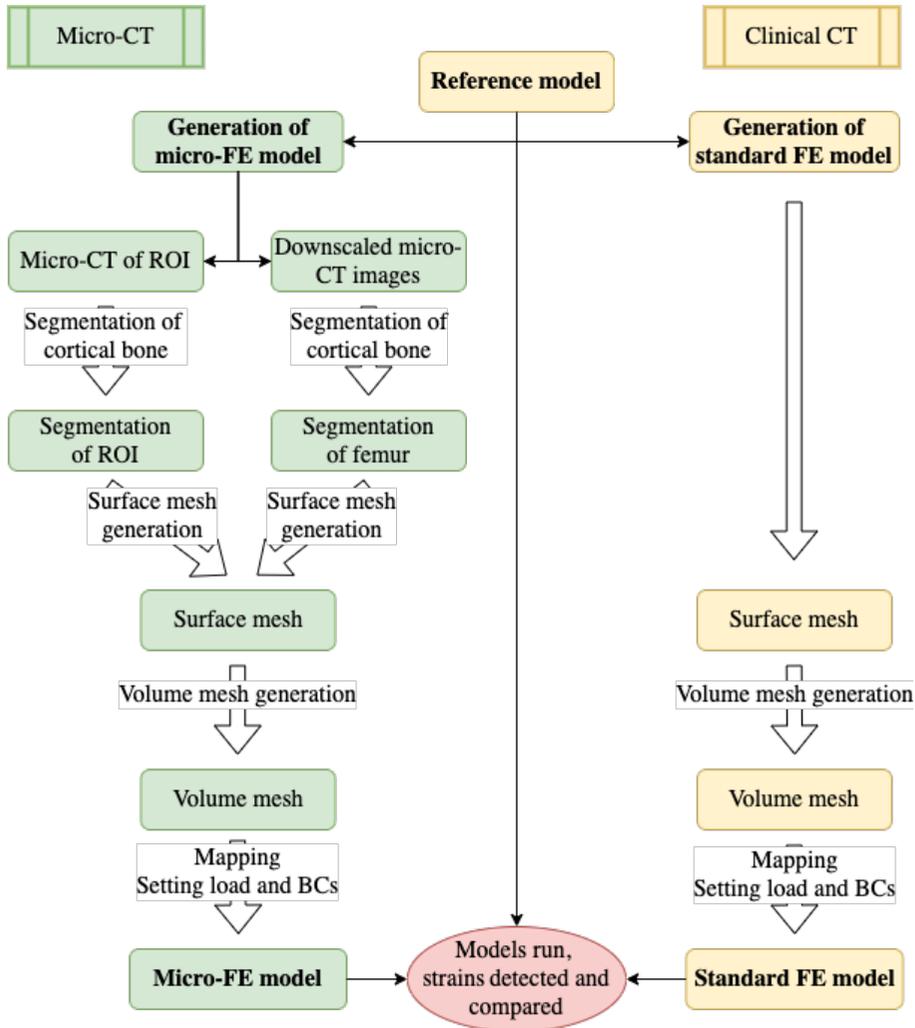
Figure 3.4: Flowchart over the generation of a micro-FE model and an overview of the FE models used for comparison and validation.

3.3   Quantification of vessel holes in micro-CT

3.3.1   ROI in micro-CT image

The aim of quantifying the vessel holes by location and size, based on the micro-CT image required the full resolution micro-CT image to be investigated. The total micro-CT scan, in full resolution, could not be handled by the computer's RAM memory. Due to this constraint, a region of interest (ROI) of the micro-CT image was selected.

The ROI was selected as a region in the femoral neck, see Figure 3.5. The placement of the ROI was based on previous studies where vessel holes have been identified [22, 21], and FE models from previous studies [10]. The FE models showed high strains in the superolateral region of the femoral neck. The ROI selection was also based on segmentation of the femoral neck surface in full resolution micro-CT images. The ROI had the size of 888x318x340 pixels, and is visualized in Figure 3.5.

(a) Coronal view.   (b) Sagittal view.   (c) Axial view.
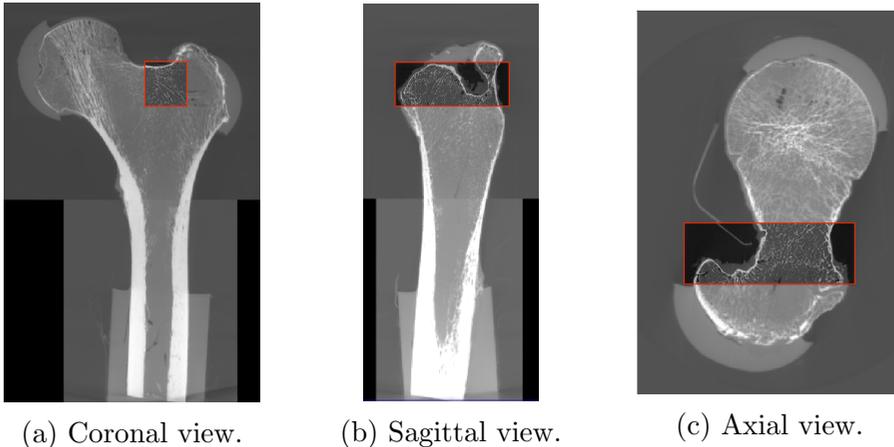
Figure 3.5: Visualization of ROI in the femur, marked with red boxes. The ROI in full resolution micro-CT images, and rest of the femur in micro-CT image re-sized by a factor 8, resulting in an isotropic voxel size of 0.444 mm.

3.3.2   Active contour segmentation of ROI

The ROI contained a region of the cortical bone surface where vessel holes were present. To obtain the vessel hole data by size and location,

the vessel holes had to be defined. The next step was therefore chosen to be, active contour segmentation, which is a method that can segment structures and contours in an image. It resulted in a segmentation of the cortical bone surface contours, including the in-growth canal structures of the vessel holes in the cortical bone.

The segmentation was performed based on the 3D contour segmentation method *Geodesic Active Contours* [34, 35]. A speed map was set up by thresholding, and resulted in a segmentation of non-bone tissue. The PDE function's parameters (equation 2.1), α and β, are both set to 1, to end up with the *Geodesic Active Contours* method. The speed-up factor was set to 10 and the initialization seeds were placed outside the femur surface (Figure 3.6). The segmentation was performed in the software ITK Snap (Version 3.8.0) [33].

The contour segmentation resulted in a surface mesh of the ROI's cortical bone structure in detail. The image edges of the ROI crop bordering to any non-bone tissue were included in the contour mesh as a by-product. The non-bone bordering edges in the surface mesh were removed.
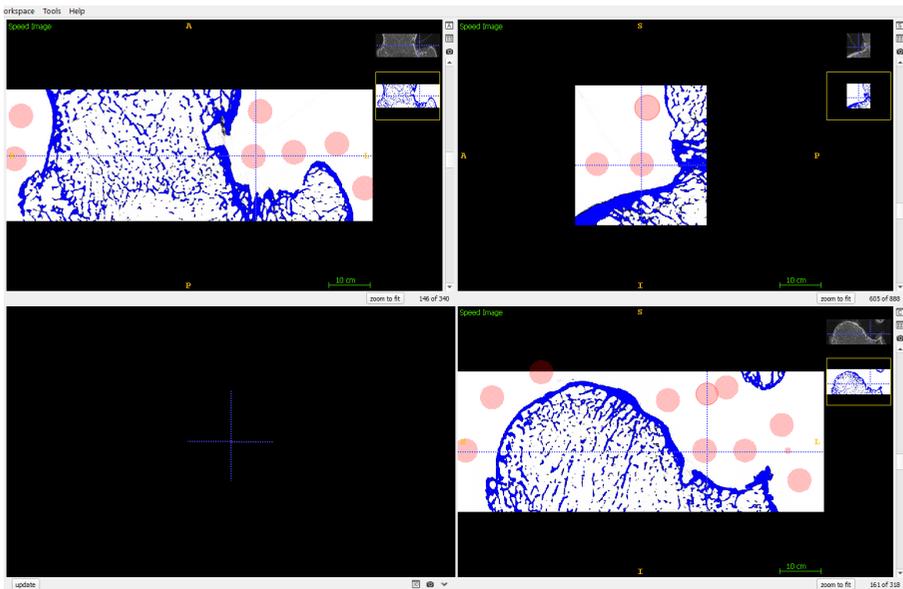

Figure 3.6: Speed map set up and initialization seeds of the 3D active contour segmentation shown in one image slice of the micro-CT ROI in ITK Snap.

3.3.3   Surface mesh generation of femur

Resampled micro-CT

The other branch of the micro-CT based approach was to generate a
surface mesh of the femur, Figure 3.3. Due to computational constraints
with the full resolution micro-CT image, and with the aim of a surface
mesh without cortical bone details, a micro-CT image downscaled by a
factor 8 was used for the surface mesh generation of femur.

Segmentation of cortical bone

The next step in building the femur surface mesh was to generate a 3D
geometry of the femur surface. The micro-CT image of the femur was
imaged with a pot around the femur's most distal part. The femur was
imaged in several sessions, resulting in different grey value distributions
in the image, see Figure 3.5 for example. Therefore, the image was
separated into two parts, by cropping it approximate with the bottom
part as 1/3 and the top part as 2/3 of the image, viewed in the sagit-
tal plane, to simplify thresholding with the varying grey values. The
segmentation was stepwise performed in the software Seg3D (Version
2.4.4) [46]. Firstly, the femur's cortical bone was segmented by thres-
hold segmentation. Secondly, the segmentation of the cortical bone was
filled. By dilation and erosion of the segmentation the holes in the tra-
becular bone were filled. Using this approach, a solid 3D-geometry was
obtained, representing the femur surface.

Mesh generation

The last step to obtain the femur surface mesh was to generate a mesh
of the 3D-geometry from the segmentation. To obtain a representation
of the femur surface, the two segmentations, the top and bottom parts
of the femur were combined to one solid part, thereafter the surface
was sculpted to a smooth and even surface, and at last remeshed with
preserved mesh density. This was performed in the software Meshmixer
[47].

3.3.4   Intersection method

The aim in the intersection method was to obtain a surface of where the
ROI contour mesh (which had the geometry of the vessel hole canals)

and the femur surface mesh intersected, crossed each other. The final intersection surface was aimed to represent the vessel holes' in-growing canals, in the cortical bone. The intersection method contained three main steps, mostly executed in Matlab (Version R2018a, MathWorks, Natick, NA, USA), using the toolbox *iso2mesh* [48] and in-house FE mesh functions.

Shrinked surface mesh of femur

In theory, two surfaces of the same cortical bone should be aligned and intersecting almost everywhere, therefore it was concluded that the intersection between the ROI contour mesh and the femur surface mesh was not a good representation of the vessel hole canals. Because of this, the femur surface mesh was first adjusted. To obtain the most descriptive representation of the vessel holes' characteristics in the cortical bone, an investigation of the role of the femur surface in the intersection method was performed. The femur surface mesh was therefore modified by decreasing its volume with different ratios, resulting in the femur surface shrinking inwards, along the surface normal. This was performed in Meshmixer, Autodesk. The volume decrease of the femur surface mesh resulted in five new surface meshes, each corresponding to different distances of shrinking along the surface normal, 0.125 mm, 0.25 mm, 0.5 mm, 1 mm, and 2 mm. The original femur surface and the femur surface shrunk by 2 mm are visualized in Figure 3.7, as an example of the concept.

Intersection of femur surface and ROI mesh

To obtain the quantification data of the vessel holes, the next step was to calculate the intersection of the ROI contour mesh and the shrunk femur surface meshes. The purpose with the intersection surface, where the meshes did cross each other, was a representation of the contours of the vessel hole canals. A visualization of the intersection concept is shown in Figure 3.8. The intersections between the five shrunk femur surfaces, and the cropped ROI contour mesh were calculated in Matlab, with the function *Surface Intersection* [49]. The resulting intersections were investigated and evaluated before proceeding. The best apparent outcome was achieved at depths of 0.125 mm, 0.25 mm, and 0.5 mm. A combination of these three intersection depths was the final intersection result.
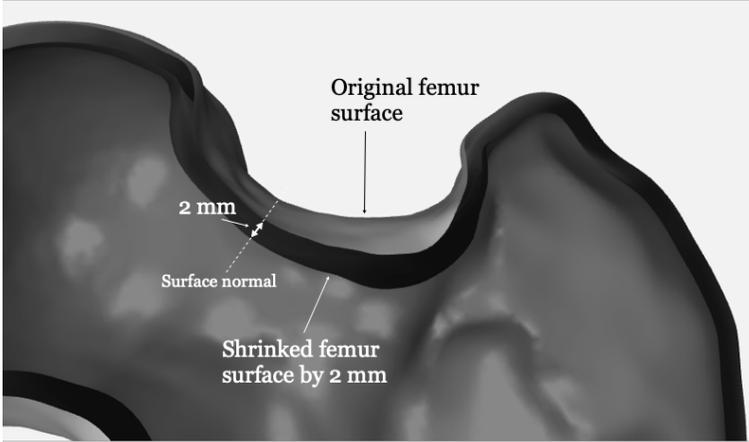
Figure 3.7: The original femur surface and the by 2 mm shrinked femur surface.
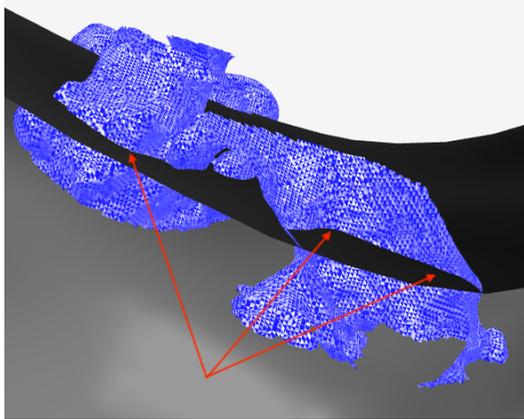
Figure 3.8: Visualization of intersection between two surfaces: the blue, here an example of a contour segmentation of a vessel hole (the canal of the vessel hole), and the black surface representing a shrunk femur surface. The area where the two surfaces cross each other is the intersection surface between the two meshes. A few examples of the surfaces intersecting are pointed out by the red arrows.

To decrease the computational cost, elements and nodes of the ROI contour mesh that were too far from the femoral surface to possibly

intersect it were removed from the calculation. This was done with an in-house Matlab code based on the function *PointInsideVolume* [50].

Due to computational constraints, the ROI was decreased to a smaller region, from now on referred to as the final ROI. The final ROI was the most superolateral region in the femoral neck, the region on the femoral neck close to the greater trochanter. This region included the most pronounced vessel holes in the contour segmentation of the ROI, and corresponds very well with the region of where the previous FE models predicted high strains in the femoral neck.

Removal of false intersection

The last step in the intersection method was to determine the true intersections and exclude any false intersections. False intersections could for example occur when the final ROI contour mesh and the shrunk surface mesh intersect somewhere where there is not a vessel hole (Figure 3.9). The surface mesh intersected with the final ROI contour mesh in areas not representing the actual in-growth of the contour evolving into the cortical bone through vessel holes. The removal of false intersections was performed in Matlab by verification of node connection in the final ROI contour mesh. Reference nodes were selected in the final ROI contour mesh, one in each intersection, and one at the contour mesh surface where no vessel holes were present. One intersection surface was controlled at a time. The surface intersection currently investigated, was saved in the final ROI contour mesh, while nodes in the other intersection areas were removed in the final ROI mesh. The node connection between the current intersection reference node and the surface mesh's reference node, was verified. If the connection did not exist, the current intersection surface was false. An example of the process of removal of false intersections is visualized in the bottom part of Figure 3.9. Also, an example of nodes in a true intersection is visualized in Figure 3.10b.

3.3.5 Circle fit

To obtain the vessel hole quantification data, the true intersections (Figure 3.10b) were fitted to circles, to obtain a simple but accurate representation of the size and location of the vessel holes. To determine the vessel holes from the true intersections, constraints about circularity were implemented to the circle fit. First, the maximum distance
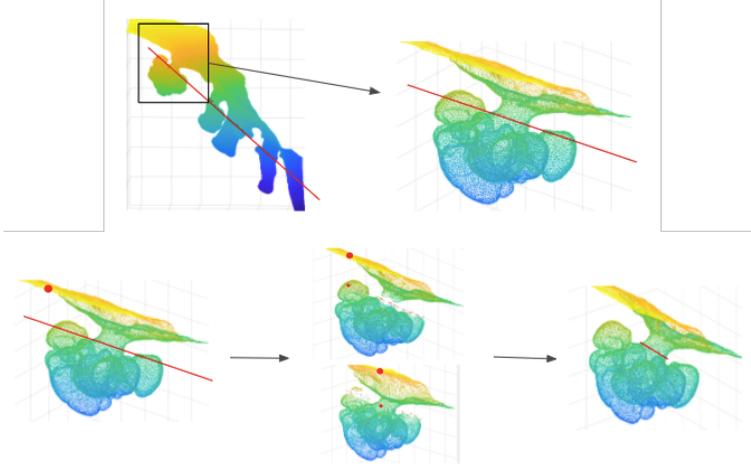
Figure 3.9: Visualization of the removal of false intersections. Top part: an example of how false intersection could occur in the ROI contour mesh. The broccoli shaped part of the mesh intersects in several regions, which not are a vessel hole canal. Bottom part: visualization of the process of how the false intersections were removed, by checking node connectivity in the mesh, resulting in the true intersection. The colors are for visualization.

between two nodes in an intersection being at least two times the radius of the fitted circle. Secondly, 75% of the nodes being placed in the area ±25% of the fitted radius, see Figure 3.10a. The circle fit, with additional constraints, was performed with an in-house Matlab code, based on the function *Best fit 3D circle to a set of points* [51].

3.3.6   Quantification

The quantified data on the vessel holes contained location and radius of the circles fitted to the true intersection holes. The three chosen depths, 0.125 mm, 0.25 mm, and 0.5 mm, were then combined to get the final result. All holes in the three intersection depths were included, and in overlapping holes found in more than one depth, the average radius and center of location of the circles were calculated as the final hole result.
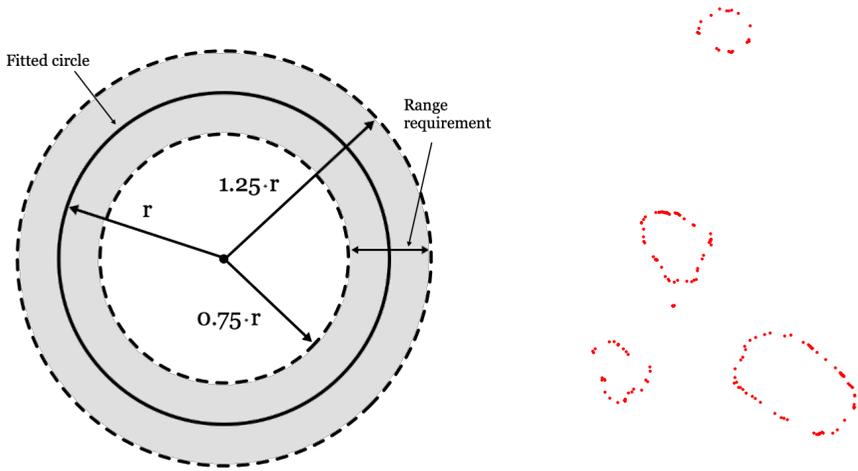
(a) Circularity constraint.

(b) Nodes in a true intersection.

Figure 3.10: (a) visualization of one circularity constraint, 75% of the nodes in the true intersection must lie within the range ±25% of the fitted circle's radius. (b) an example of nodes in a true intersection between the ROI contour mesh and a shrunk femur surface mesh.

3.4 Quantification of vessel holes in clinical CT

3.4.1 Clinical CT images

A clinical CT scan was used in this project, reconstructed with two different kernels, one smooth kernel and one hard kernel (Figure 3.2). The clinical CT images have a voxel size of 0.42 mm. With the resolution the clinical CT images have, it is not possible to clearly see holes in the cortical bone. This approach was based on the idea of investigating the cortical bone thickness, and by detecting thin, or non-valued cortical bone thickness, vessel holes could be detected.

3.4.2 Segmentation and mesh generation of femur surface

The first step in the clinical CT based approach was to segment the cortical bone surface by thresholding. The result of the segmentation was

a 3D geometry, represented by a surface mesh of the femur. The mesh contained 18 949 nodes, with an average distance between the nodes of 0.34 mm. Considering that Stradview calculates the thickness only on a random uniform sample of the available nodes [52], it was considered there might be a risk for some vessel holes to be not detected because the algorithm would not probe densely enough. Therefore, a more dense 3D mesh, with 75 800 nodes, and the average distance between the nodes of 0.17 mm, was generated. The 75 800 node mesh was created by a modification of the 18 494 node mesh in Matlab, by the function *Triangle Subdivide (vectorized/fast)* [53]. The segmentation and mesh generation of femur surface in the clinical CT images was performed in Stradview (Version 6.05, Medical Research Imaging Group, Cambridge University, Engineering Department) [36].

3.4.3   Calculation of cortical bone thickness

The next step in the clinical CT approach was to calculate the cortical bone thickness in the femur. The calculation of the cortical bone thickness was performed with the technique *Cortical Bone Mapping (CBM) v2* [37], in Stradview. The thickness was calculated on a random uniform sample of the nodes in the 3D mesh along a line crossing the cortical bone, see Figure 3.11. The line was determined to have a width of 0, as it otherwise smoothens the thickness calculation, which was not desired.

Three different line lengths were examined (4 mm, 6 mm, and 8 mm), based on the assumption that the cortical bone thickness in the femoral neck does not exceed 2 mm. The line length is recommended to be three times longer than the expected thickness [36].

This resulted in an investigation of 12 combinations of cortical bone thickness results, including three line lengths, two reconstruction kernels, and two different node densities of the surface mesh.

The results were 3D surface meshes of the cortical bone's outer and inner surfaces, and thickness data mapped to every node in the surfaces. See Figure 3.12 for an example window of Stradview.

3.4.4   Quantification

The last step in the clinical CT based approach was the quantification, of location and size of the vessel holes.

(a)

(b)
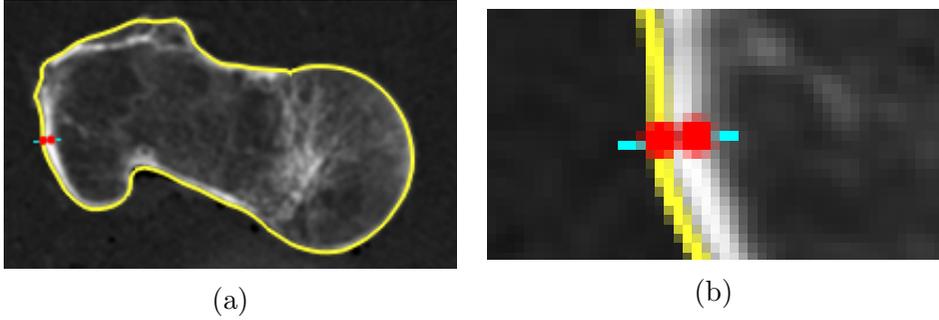
Figure 3.11: Example of thickness calculation of the cortical bone, where the thickness is calculated in all nodes of the surface mesh, represented by the yellow line. The blue line represents the line of where the thickness was calculated along. The red dots mark the inner and outer surface of the cortical bone, resulting in the thickness. To the left, the whole femur. To the right, zoomed in on the line.
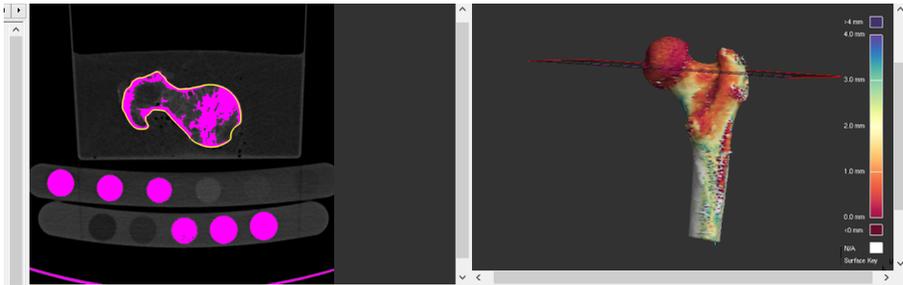

Figure 3.12: An example of Stradview. To the left, the yellow line representing the 3D mesh of the femur, which was based on the pink segmentation. To the right, the 3D mesh of the femur is mapped to its cortical bone thickness. The different colours represent the measured cortical thickness.

To identify vessel holes, we defined the minimum allowed cortical thickness to be 0.2 mm. This threshold was based on a visual investigation of our images. Consequently, every point with a calculated thickness < 0.2 mm (or failed thickness calculation) was marked as a vessel hole. The vessel hole quantification was based on the number of node holes connected in the surface mesh. Three different classes of node holes were quantified. The three approaches are presented in Table 3.1. Isolated nodes were single nodes classified as holes. Paired nodes were two nodes connected in the mesh, classified as holes. Cluster

nodes were 3 or more connected nodes classified as holes.

The first two classes, isolated and paired nodes, were quantified in terms of location, and by the average distance (ad) between two nodes in the mesh. In the third class, the node holes were fitted to circles, similar to the micro-CT based approach, with the Matlab function *Best fit 3D circle to a set of points* [51]. The quantification of vessel holes in the clinical CT was performed in Matlab.

Class	#nodes	Location	Radius
Isolated nodes	1	Node location	ad * 1/2
Paired nodes	2	Avg. node coord.	ad * 2/3
Cluster nodes	≥3	Circle center	Circle radius

Table 3.1: Quantification of the three different classes of holes. The two first classes are quantified in terms of location and the average distance (ad) between two nodes in the mesh. In the third class the nodes are fitted to circles, as in the micro-CT based approach, but without the constraints.

3.5   Evaluation of vessel hole quantification

The evaluation of the two approaches, the micro-CT based method and the clinical CT based method, was first done visually by examining performance accuracy and by comparing the holes' size and location, using the micro-CT result as a reference. The performance accuracy, in terms of number of holes and hole location, was calculated according to

$$Accuracy = \frac{TN + TP}{TN + TP + FN + FP} \tag{3.1}$$

where TN = true negative, TP = true positive, FN = false negative, and FP = false positive. The TP was the correctly quantified holes in terms of location, FN was the never detected holes, FP was the falsely detected holes, and TN was considered as zero since there were no correctly non detected holes.

3.6 Generation of FE models

This section describes the procedure to generate the micro-FE model and the standard FE model. The first step of generating a surface mesh was different for the two FE models but apart from this the procedure was the same.

3.6.1 Surface mesh of micro-FE model

The aim of this step was to obtain a surface mesh of the femur, representing the cortical bone surface, including the vessel hole structure in the femoral neck. Due to computational constraints it was not possible to use the total micro-CT image in full resolution be the basis of the femur surface mesh. To select and generate the best possible mesh, an image resolution investigation was performed.

Image resolution

The image resolution investigation was performed to find the most representative mesh of the femur required in this part of the project. By reducing the micro-CT image size in three steps, the resolution was decreased and visually investigated. The image was rescaled by factors 2, 4, and 8 in ImageJ [54], resulting in four images with different resolutions. The rescaled micro-CT is presented in terms of data in Table 3.2 and visually in Figure 3.13.

Scale factor	Image size [pixels]	Pixel size [mm]
1	1394 x 2000 x 3110	0.0555
2	697 x 1000 x 1555	0.111
4	348 x 500 x 776	0.222
8	175 x 250 x 387	0.444

Table 3.2: Rescaled image data in the resolution investigation. The micro-CT image scaled by different factors, including the full resolution image with scale factor 1.

The region depicted in Figure 3.13 were segmented. Based on the segmentations a resolution investigation was done. After visual evaluation, it was decided that the majority of the femur could be represented

(a) Full resolution.

(b) Scaled by 2.

(c) Scaled by 4.

(d) Scaled by 8.
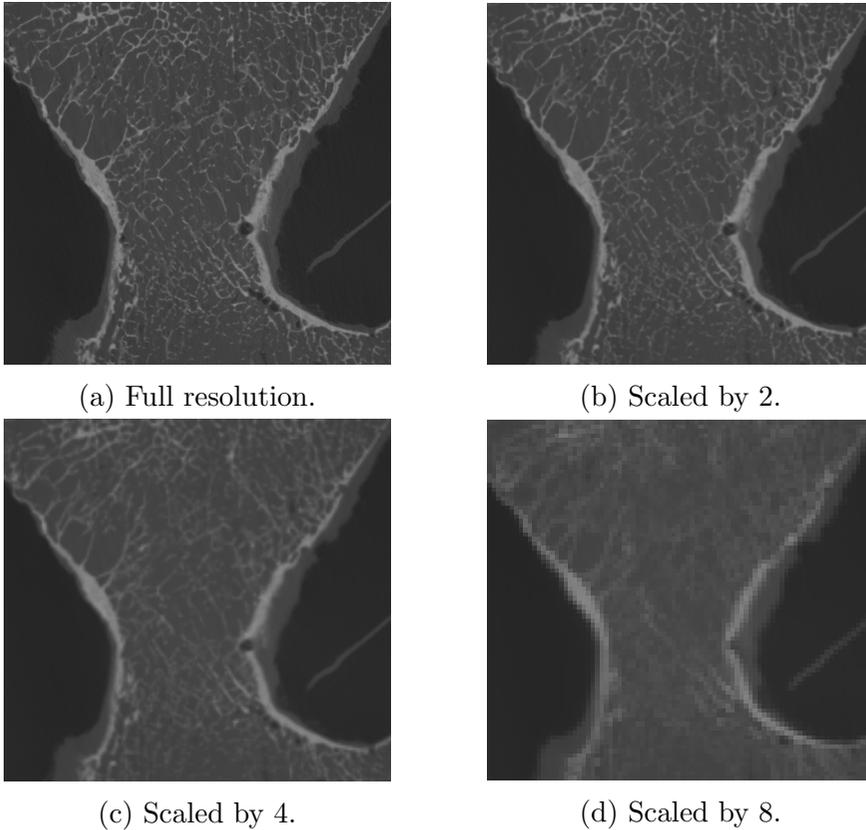
Figure 3.13: Visualisation of one slice of each resampled micro-CT image of the femoral neck, image and pixel size according to Table 3.2.

by the micro-CT images downscaled by a factor 8. The region of interest in the femoral neck in this part of the project was the ROI presented in subsection 3.3.1, chosen to be based on the full resolution micro-CT image.

Segmentation and mesh generation

The main femur surface mesh, built as a first step of the FE model generation, consists essentially of the downscaled by a factor 8 micro-CT image. Additionally, the femur surface mesh also contains a segmentation of the ROI, based on a full resolution micro-CT image. The rescaled micro-CT image was segmented to obtain the femur surface as a solid 3D geometry, with the same approach used in section 3.3.2. Due to varying grey values in the micro-CT image, the femur was segmented

in two parts, resulting in a top and a bottom part. The segmentation of the full resolution ROI was performed with the aim to segment the cortical bone structure in detail, since it is the region where vessel holes are present and the region of interested in this project. The focus of the ROI segmentation was the cortical bone structure. The trabecular bone was removed in the ROI segmentation and replaced with the segmentation of the femur surface based of rescaled micro-CT images. The segmentations were performed in Seg3D.

Figure 3.14a shows the different segmentations, where the green and red parts are segmentations based on the resampled micro-CT images, rescaled by factor 8, see Table 3.2. The blue part of the segmentation shows the ROI and has full micro-CT resolution. In this segmentation the vessel holes at the femoral neck are visible (Figure 3.14b).


(a) Full femur.

(b) Femoral neck.
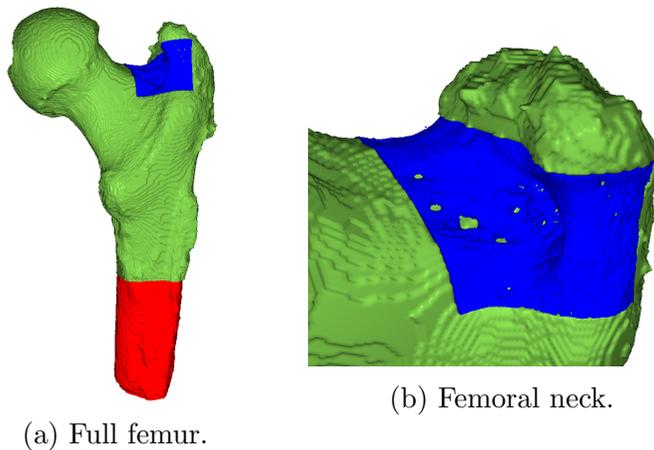
Figure 3.14: Visualization of the three segmentations. Blue: segmentation of ROI with full micro-CT resolution. Green and red: segmentation of femur performed with resampled micro-CT images.

The three segmented parts were combined, smoothed, and a solid femur mesh was created in Meshmixer. The result was a surface mesh of the femur with the ROI in more detail, and is shown in Figure 3.15.

3.6.2   Volume mesh of micro-FE model

The surface mesh is shown in Figure 3.15 and, as seen in subfigures 3.15b and 3.15c, the mesh density is high enough to capture the shape of the vessel holes. In total, the surface mesh of the full femur, Figure

3.15a, had about 594 000 triangular elements. The surface mesh was sequentially re-meshed keeping the mesh density high around the ROI but lowering the mesh density away from the ROI.

(a) Full femur.   (b) Femoral neck.   (c) Vessel hole.
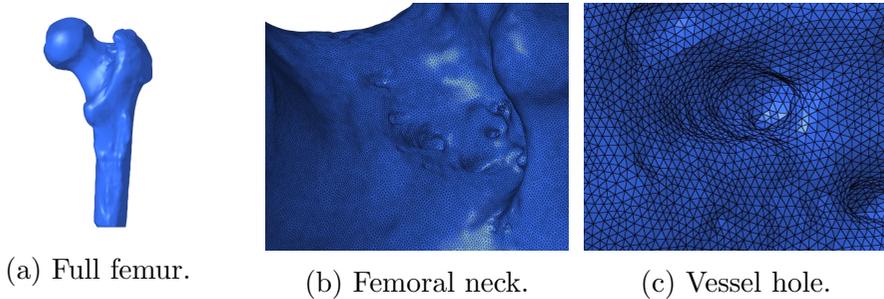
Figure 3.15: Surface mesh generated based on full-resolution micro-CT images and resampled micro-CT images. Surface mesh of the full femur (a), the femoral neck (b), and a vessel hole (c).

The re-meshing was performed with the software Hypermesh [55]. By selecting the femur excluding the femoral neck a new surface mesh could be created stepwise, with increasingly large elements further away from the ROI. The final surface mesh is visualized in Figure 3.16 and has about 73 000 triangular elements. The smallest elements are about 0.25 mm and the largest elements are about 3 mm.
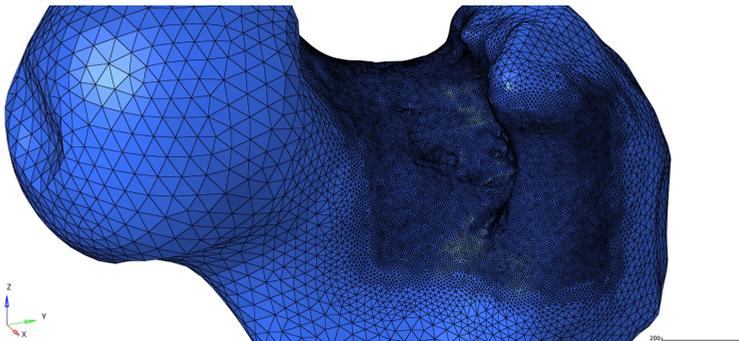

Figure 3.16: Femoral neck of re-meshed surface mesh showing how the element density gradually decreases away from the ROI.

From the surface mesh a volume mesh was generated using the option tetra-mesh with settings growth rate = 1.3, pyramid to transition = 0.8 and number of layers = 2 resulting in a mesh consisting of about 656 000 ten-node tetrahedral elements.

3.6.3 Mesh generation for standard FE model

The starting point for the standard FE model was a set of surfaces that has previously been generated from clinical CT images. The surfaces are shown in Figure 3.17a. The surfaces were meshed individually with different mesh densities. The mesh was made so that the mesh density was the highest in the region of the femoral neck and lower in the shaft of the femur as shown in Figure 3.17b.



(a) Set of surfaces. (b) Surface mesh.
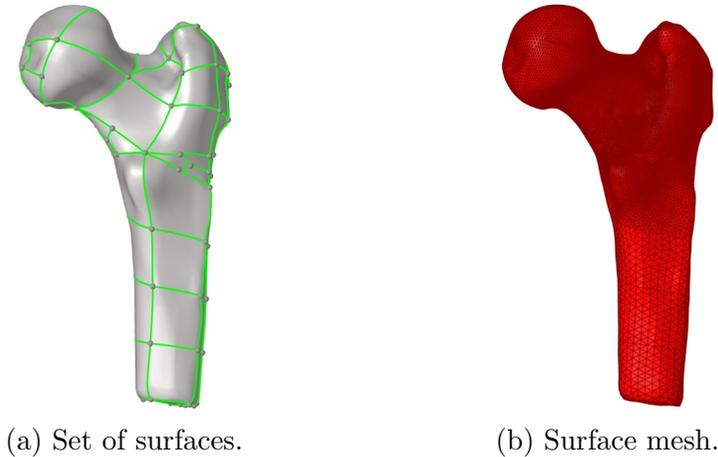
Figure 3.17: Set of surfaces and resulting surface mesh describing the standard FE model.

From the surface mesh a volume mesh was generated in the same way as for the micro-FE model. The volume mesh had a total of about 254 000 ten-node tetrahedral elements.

3.6.4 Mapping

The mapping of material properties onto elements for the micro-FE model and the standard FE model was performed using both micro-CT images of full resolution and clinical CT images. The reason for not mapping the full femur with micro-CT images was large computational time. Figure 3.18 shows what part of the mesh was mapped with clinical CT and micro-CT images.

The calibration of the clinical CT images was already available, and for the micro-CT images, the calibration was performed by measuring the pixel value for six phantoms with known ash density. This was done on ten images and an average pixel value was determined for each
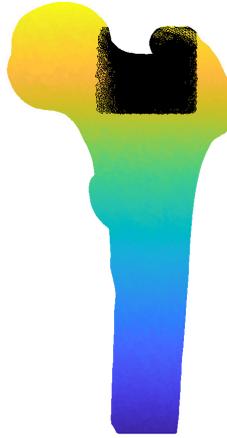
Figure 3.18: The mesh marked in black is mapped with micro-CT images and the rest of the femur is mapped with clinical CT images.
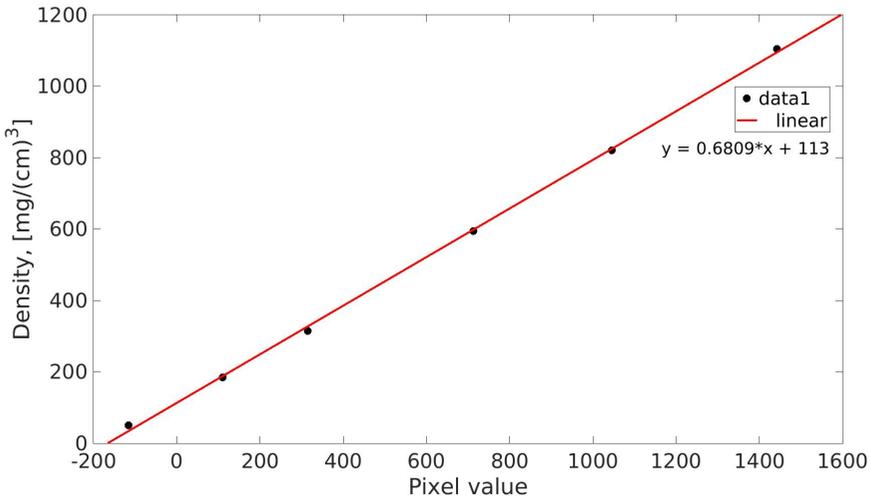
Figure 3.19: Showing the calibration of micro-CT images. The pixel value is measured for six phantoms with known ash-density resulting in a linear relationship between pixel value and density for the micro-CT images.

phantom. By doing a linear regression of the pixel value vs. density, a linear relation was found (Figure 3.19). In this way the pixel value for a certain element could be translated into a value for its density.

The coordinates of each element are mapped to the corresponding co-
ordinates in the CT image stack. An average grey value is determined
for each element and translated into a density value (Figure 3.20). All
density values were subsequently converted to Young's moduli following
Equation 2.4.

(a) Cross section of the femur shaft.

(b) Corresponding CT-image.
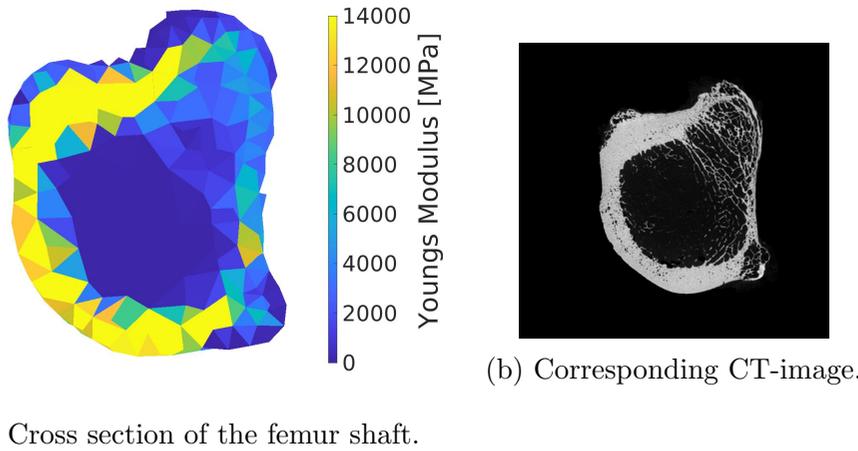
Figure 3.20: Young's modulus in MPa mapped to each tetrahedral ele-
ment based on the grey-value of the corresponding CT image.

3.6.5 Boundary conditions

After a volume mesh was generated and each element was mapped to the
corresponding value of Young's modulus the positioning of the femur,
the load and the boundary conditions were set. The simulation is of a
sideways-fall, and the aim of setting load and boundary conditions was
to replicate the experimental conditions. The femur was fixed at 10°
adduction, 15° internal rotation to represent the the experimental setup
[14] and the femur was fixed at the distal end of the shaft and at the
lateral side of the head (Figure 3.21). In the shaft, nodes 50 mm or less
from the most distal node, was fixed. At the lateral side of the head,
nodes 5 mm or less from the most lateral node was fixed. The load was
applied on the external nodes of the femoral head located 5 mm of less
from the most medial node, and with a magnitude of 2250 N divided
on the number of nodes at which the force was applied. The choice of
force was based of the predicted fracture force in the reference model.
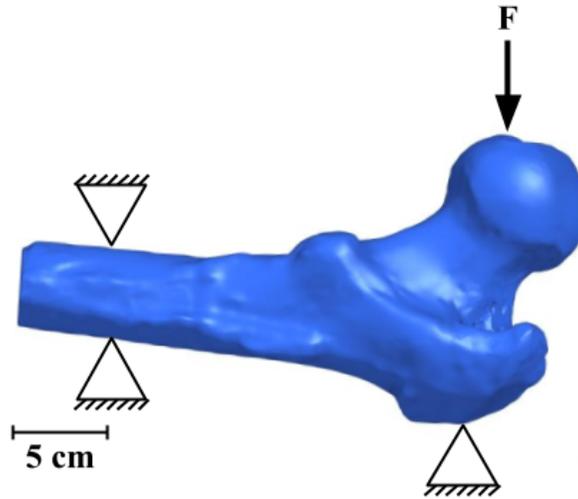
Figure 3.21: Sketch of how the boundary conditions and load were applied. Femur is fixed at the shaft and at the lateral side of the head, and the force is applied at the medial side of the head to simulate a sideways fall.

3.6.6   Simulation

The simulations of the sideways fall were performed using the software Abaqus/CAE 2018 [56]. A linear model was used applying a load as described earlier fixing the nodes at the BCs in all directions. After the simulation the major principal strains and the minor principal strains were saved, both for individual nodes and element centroids.

3.7   Validation of the micro-FE model

This chapter will describe the procedure of validating the quality of the micro-FE model and how the results can be compared to other models and to experimental data. Figure 3.22 is an overview of the models used for validation, how modelling parameters are investigated and how the models are later compared.

3.7.1   FE models used for validation

Validating the micro-FE model was performed comparing it to the standard FE model and the reference model. The meshes of the three mod-
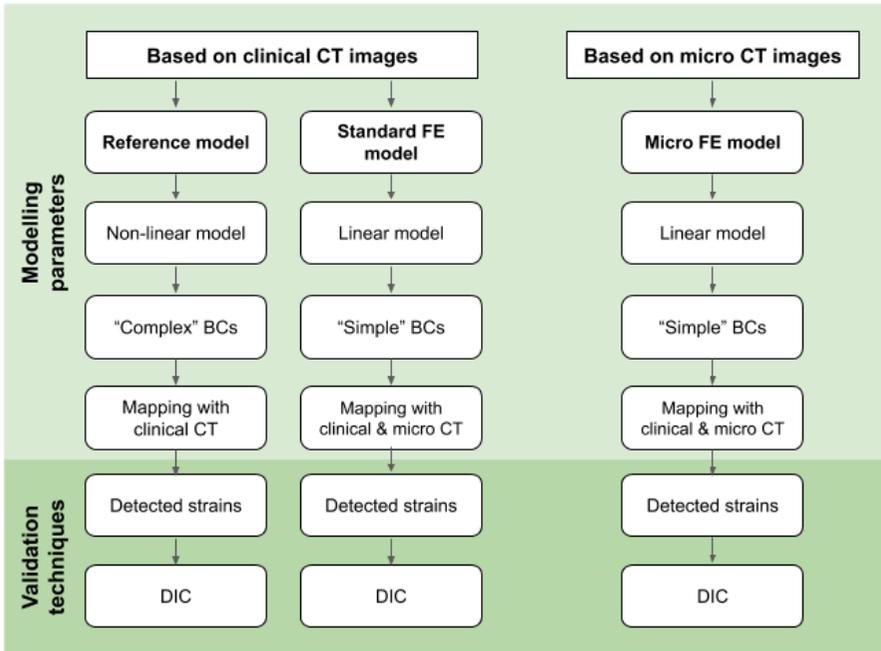
Figure 3.22: Overview of the FE models and validation techniques introduced for the validation.

els can be compared in Figure 3.23 and a summary of the number of elements and approximate element size can be found in Table 3.3.


(a) Reference model   (b) Standard FE model   (c) Micro-FE model
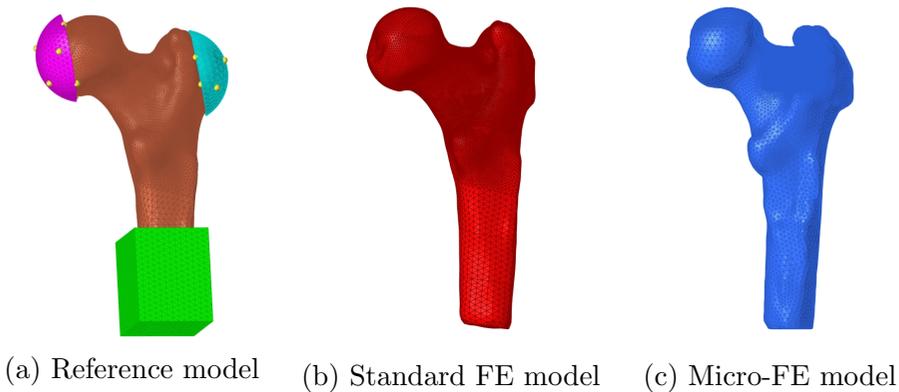
Figure 3.23: Overview of the FE models used for validation.

Model	#elements	Element size at neck [mm]
Reference	171760	1
Standard FE	253858	0.81
Micro-FE	656391	0.31

Table 3.3: Summary of the number of elements and approximate elements size at the femoral neck for the FE models.

Reference model

The reference model has previously been developed and validated by our group at the Department of Biomedical Engineering and is based on the FE-model introduced by Grassi et al. (2016) [10]. The shape of the mesh is based on segmentation from clinical CT images. The model is non-linear and the simulation is run until local failure according to a strain-based criterion. The BCs differ from the standard FE and micro-FE model, in the way that the shaft of the femur is fixed in a pot around it and the lateral side of the femur is fixed with a cup. The load is applied at the femoral head, which also is fixed with a cup. The model with cups and pot is shown in Figure 3.23a. The mapping of the femur is made exclusively with clinical CT images, and the elements at the surface of the mesh of the femur were assigned a minimum Young's modulus of 2.5 GPa

Standard FE model

The standard FE model has been developed by the authors as a step in between the reference model and the micro-FE model. The surface mesh was based on segmentation from clinical CT images and the mesh density was similar to the mesh density of the reference model. The model was linear and the simulation was run setting the load to 2250N distributed over the external nodes located 5 mm or less from the most medial node. The BCs were set for the external nodes 50 mm or less from the most distal part of the femur and for the external nodes 5 mm or less from the most lateral node on the femur (Figure 3.21). The mesh was mapped with micro-CT images in the ROI as shown in Figure 3.18 and with clinical CT images for the rest of the femur.

Micro-FE model

The micro-FE model had a much finer mesh than the previous two models. Apart from this, the modelling approach was the same as for the standard FE model.

3.7.2 Approach

By first comparing the reference model and the standard FE model with similar mesh density, assumed to be constant, the modelling parameters in terms of the choice of a linear model, boundary conditions and the mapping strategy was investigated. The micro-FE model had a larger number of elements and especially much smaller elements at the femoral neck. Comparing the standard FE and micro-FE models all parameters were kept constant except for the mesh. This comparison made it possible to investigate the effect of having a highly refined mesh.

3.7.3 Qualitative comparison

The resulting strains for the three models were compared qualitatively by visualizing the strains both at the femoral neck and specifically for locations of detected vessel holes. The strain distributions were plotted for each element and compared between the models. For the detected vessel holes, also an average of the strains around that vessel hole was determined.

3.7.4 Validation with DIC

Finally, the strains detected for the standard FE model and the micro-FE model were validated against experimental data obtained by Digital Image Correlation (DIC) for this specific bone. The DIC measurements were performed by our research group and have recently been published [14]. A new micro-FE mesh was created in order to have highest mesh density in the complete DIC region according to previously described procedure. Except for the mesh, the model was identical to the micro-FE model. Point clouds of the external nodes were created in Matlab, both for the standard FE model and the micro-FE model, and the nodes were aligned with the point cloud for the DIC using the software CloudCompare [57]. Figure 3.24 shows the alignment of the nodes of the standard FE model and the DIC point cloud.
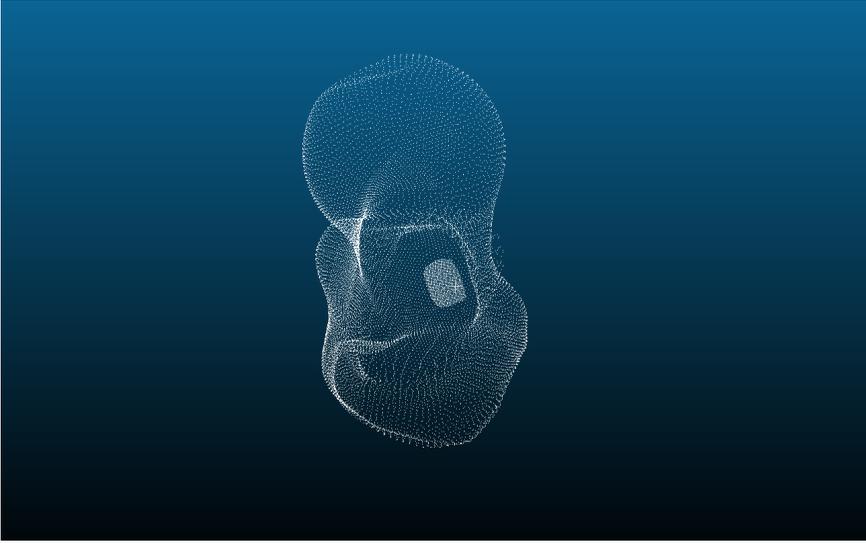
Figure 3.24: Aligning the nodes of the standard FE model with the point cloud of the DIC.

An in-house developed Matlab function was used for comparing the strains obtained experimentally with DIC and the strains detected by the FE models. The strain in each external node of the FE model were compared to the strain in DIC points at a distance related to the distance between external nodes in the DIC area. The difference between the predicted and measured strains was visualized both as a distribution on the femur and as correlation and Bland-Altman plots.

Chapter 4

Results

4.1 Quantification of vessel holes

The result from the quantification of the vessel holes in both micro-CT and clinical CT scans are presented in this section. Firstly, the micro-CT based approach results are presented by visualization, followed by the quantification data in terms of location and size of the vessel holes detected. Secondly, results of the clinical CT based approach are presented in the same order, and a presentation and visualization of the best performing combination of the clinical CT results.

4.1.1 Micro-CT

3D geometry of micro-CT ROI

The result from the first step of the micro-CT based approach was the mesh generated by the contour segmentation of the ROI (Figure 4.1). The ROI selected in section 3.3.1, visualized again below in Figure 4.2. The in-growth in the surface mesh (Figure 4.1) was the shape and structure of the vessel hole canals, from the outer surface of the femur and into the trabecular structure.

Mesh of micro-CT femur surface

The result of the femur surface mesh generation, built of the micro-CT images downscaled by a factor 8, was a smooth mesh of the femur surface (Figure 4.3). The smooth surface resulted in a coarser representation of

(a) ROI mesh
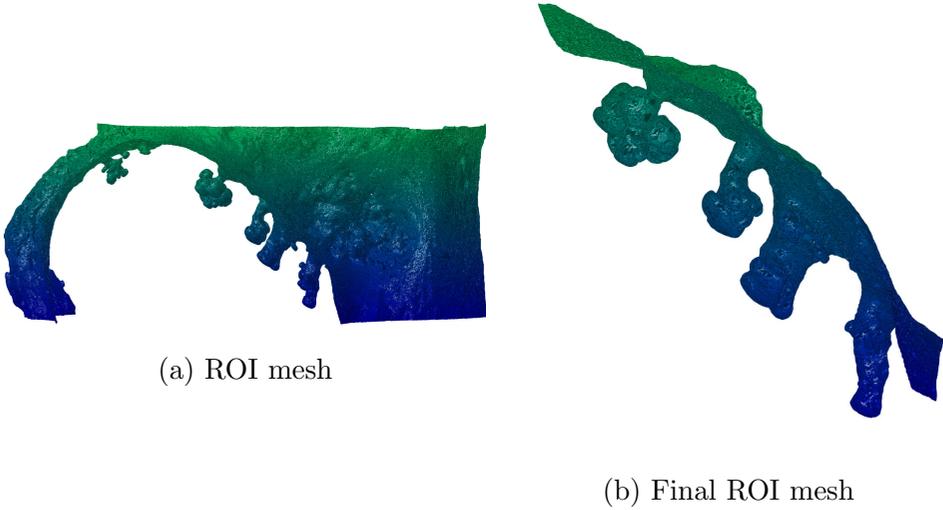
(b) Final ROI mesh

Figure 4.1: Coronal view of the contour segmentation of the ROI surface and final ROI in the superolateral femoral neck, used in the micro-CT based quantification approach. The mesh parts shaped as canals or "upside down broccoli", were where the active contour segmentation evolved into the vessel holes canals in the cortical bone. The bubbles, or "broccoli heads", were the result of when the contour started to evolve in the porous trabecular bone structure. The colors are for visualization.

(a) Coronal view.

(b) Sagittal view.

(c) Axial view.
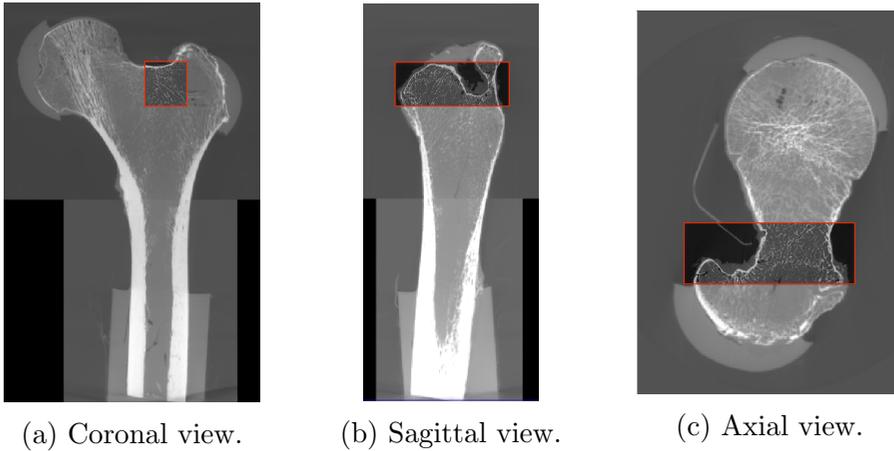
Figure 4.2: Visualization of thr ROI in the femur. The ROI in full resolution micro-CT images, and rest of the femur in micro-CT image re-sized by a factor of 8, pixel size of 0.444 mm.

the femur surface, without smaller details, but still including the main structure.

Figure 4.3: Femur surface mesh of micro-CT scan, built from a segmentation of micro-CT images scaled by a factor 8. The mesh represents a smooth femur surface, excluding very small details.

Quantification data of the vessel holes in micro-CT

The quantification in the micro-CT based method resulted in the detection of five vessel holes in the final ROI. The five vessel holes are visualized together with the femur surface mesh (generated in subsection 3.6.1) in Figure 4.4, with corresponding radius data in Table 4.1. The vessel holes are also visualized on micro-CT scan slices of the ROI, viewed in the coronal plane (Figure 4.5). The micro-CT slice chosen for each hole was based on the location data. The accuracy, in terms of number of holes detected, in the micro-CT based approach was visually determined to 1, as all holes in the region of interest were detected.

(b) The quantified vessel holes numbered.
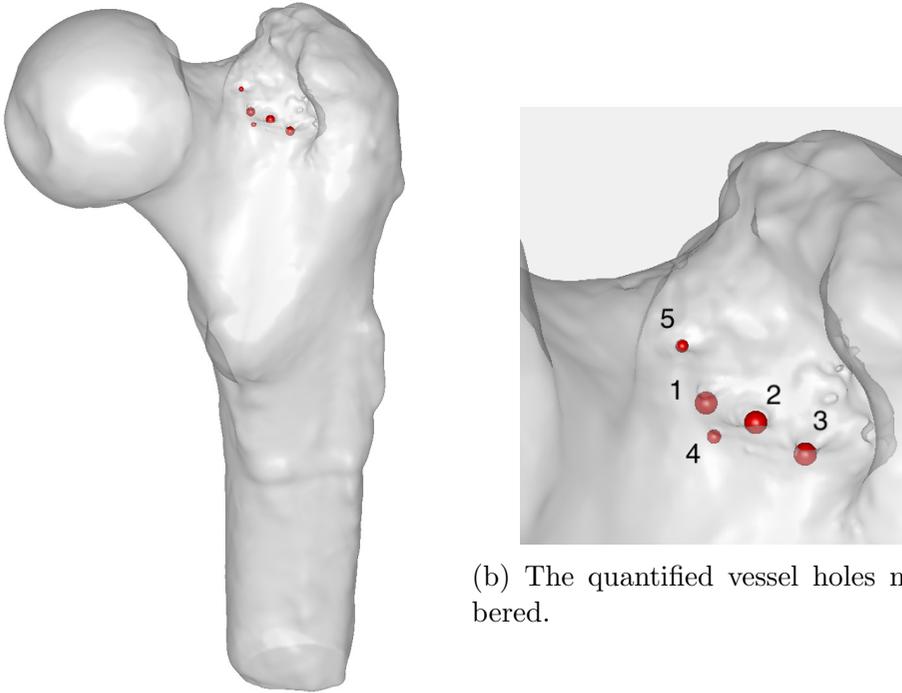
(a) Femur with quantified vessel holes.

Figure 4.4: Quantified vessel holes in the final ROI visualized together with the femur surface mesh.

Vessel hole	1	2	3	4	5
Radius [mm]	0.9843	0.9981	1.0015	0.6132	0.5587

Table 4.1: Radius of the five quantified vessel holes from the micro-CT based method.

4.1.2   Clinical CT

Surface mesh of clinical CT femur surface and cortical bone thickness

The 3D geometry, generated from the clinical CT images, was the first result in the clinical CT based approach (Figure 4.6a). The clinical CT based 3D geometry had some non-smooth surface areas, especially at the shaft, the greater trochanter, and at the head. Comparing to the
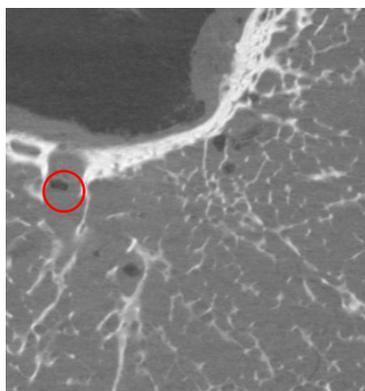
(a) Vessel hole 1.
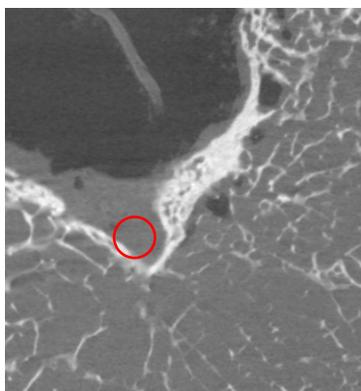
(b) Vessel hole 2.
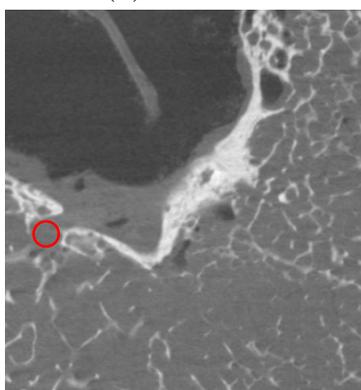
(c) Vessel hole 3.

(d) Vessel hole 4.
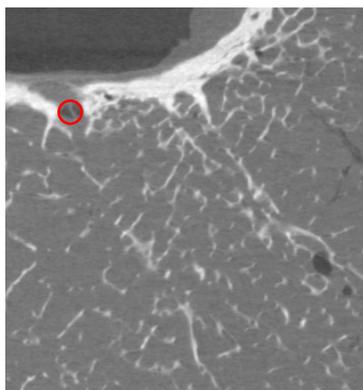
(e) Vessel hole 5.

Figure 4.5: Visualization of the quantified vessel holes shown as red circles, plotted on micro-CT image slices of the coronal view in the ROI. The micro-CT slice corresponds to the location quantified in the method. The size of the red circle represents the determined radius of each vessel hole.

micro-CT surface mesh (Figure 4.3), this geometry was not as accurate. However, at the femoral neck region the mesh did not show any clear inaccuracies.

The cortical bone thickness was mapped to the surface mesh (Figure 4.6b). In the final ROI, the cortical bone thickness was estimated within the range of 0 - 1.67 mm.
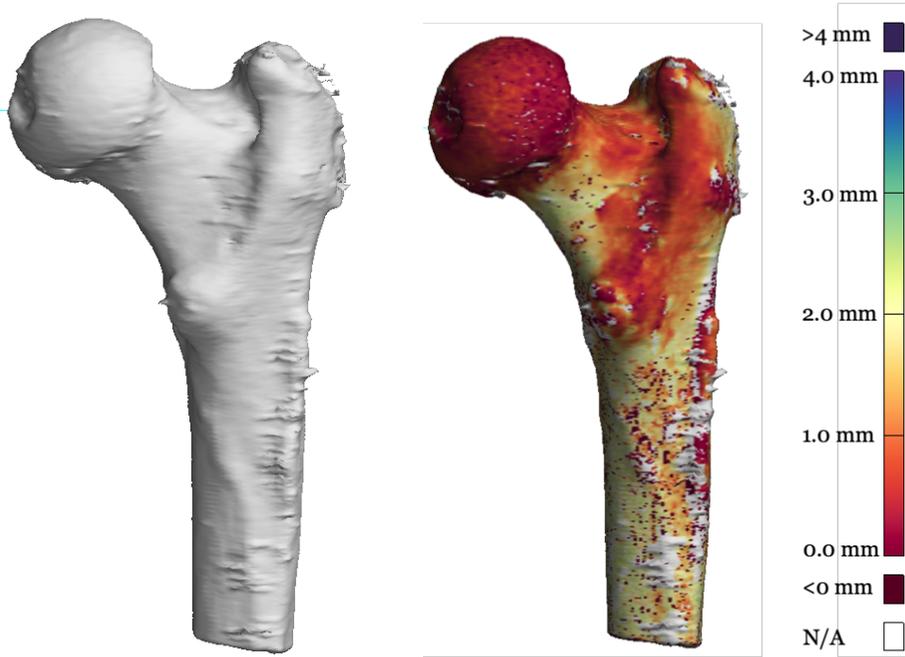

(a) 3D-geometry of femur.

(b) Cortical bone thickness in femur.

Figure 4.6: (a) the 3D geometry generated from a segmentation of the clinical CT images. (b) the cortical bone thickness mapped to the 75 800 node mesh, with setting: technique=CBM v2, line width=0, and line length=4.

Quantification data of the vessel holes in clinical CT

The first result of the quantification in the clinical CT based approach was the vessel hole quantification in the twelve combinations of different settings (three line lengths, two reconstruction kernels, and two meshes with different node densities). This resulted in twelve diverse quantification data, presented in Table 4.2, in terms of number of holes detected

for each combination. The accuracy of each combination is presented in
Table 4.3, calculated according to equation 3.1. The highest accuracy
obtained was 0.60, and the lowest was 0.20.

Scan and mesh density	line l.=4	line l.=6	line l.=8
Smooth, low dense	2	1	1
Hard, low dense	2	2	2
Smooth, high dense	3	2	1
Hard, high dense	8	10	6

Table 4.2: Number of holes detected in the clinical CT based approach,
all twelve combinations of settings presented.

Scan and mesh density	line l.=4	line l.=6	line l.=8
Smooth, low dense	0.40	0.20	0.20
Hard, low dense	0.40	0.40	0.40
Smooth, high dense	0.60	0.40	0.20
Hard, high dense	0.44	0.36	0.38

Table 4.3: Accuracy of the quantified holes in the clinical CT based
approach, all twelve different combinations of settings presented. A
high accuracy signifies more correct classified holes.

The combination that resulted in the highest accuracy was the clin-
ical CT scan reconstructed with a smooth kernel, using a high density
node mesh, and a line length of 4 mm. The result of the quantifica-
tion from this combination is visualized together with the femur surface
mesh (generated in the subsection 3.6.1), in Figure 4.7. The radii of the
quantified vessel holes are presented in the Table 4.4. The quantified
vessel holes are visualized on micro-CT slices (Figure 4.8). Note that
the clinical CT holes were not as accurately located, and were a bit off,
comparing to the micro-CT holes. They quantified holes in the both
CT scan methods were though overlapping. Vessel hole 3 (Figure 4.8c)
was overlapping the corresponding micro-CT hole by 1 mm, considering
their radii and locations.

(b) The quantified vessel holes numbered.
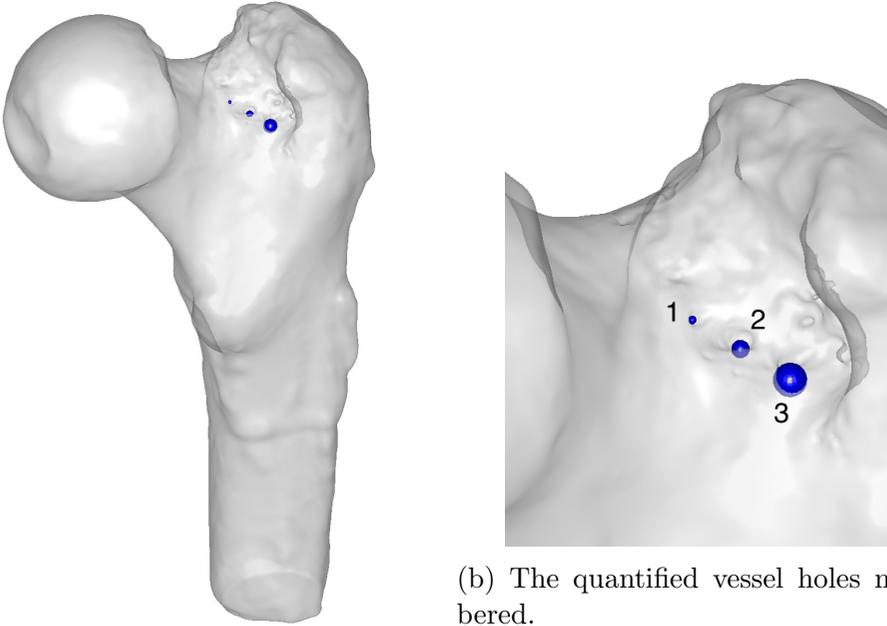
(a) Femur with quantified vessel holes.

Figure 4.7: Quantified vessel holes in the final ROI in the clinical CT scan, visualized together with the femur surface mesh.

Vessel hole	1	2	3
Radius [mm]	0.4044	0.8741	1.6376

Table 4.4: Radius of the three quantified vessel holes from the clinical CT based method.

4.1.3   Evaluation

The evaluation of the quantification of vessel holes are presented in this section. The final result from both the micro-CT and the clinical CT approach are depicted together in Figure 4.9. The three vessel holes detected by the clinical CT method overlapped with vessel holes detected by the micro-CT method.
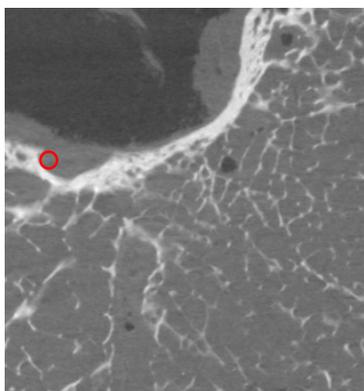
(a) Vessel hole 1.
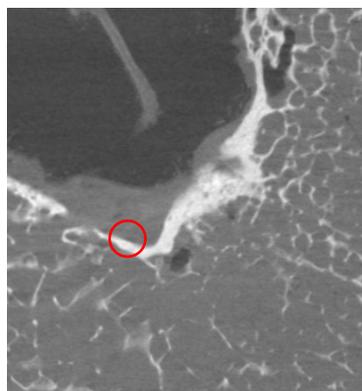
(b) Vessel hole 2.
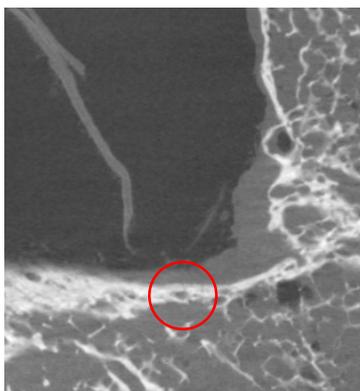
(c) Vessel hole 3.

Figure 4.8: Visualization of the quantified vessel holes in the clinical CT based approach shown as red circles, plotted on micro-CT image slices of the coronal view in the ROI. The slice selection of the micro-CT images, for each vessel hole, was based on the clinical CT based vessel hole location data, and the size of the red circle was the radius of the vessel hole.
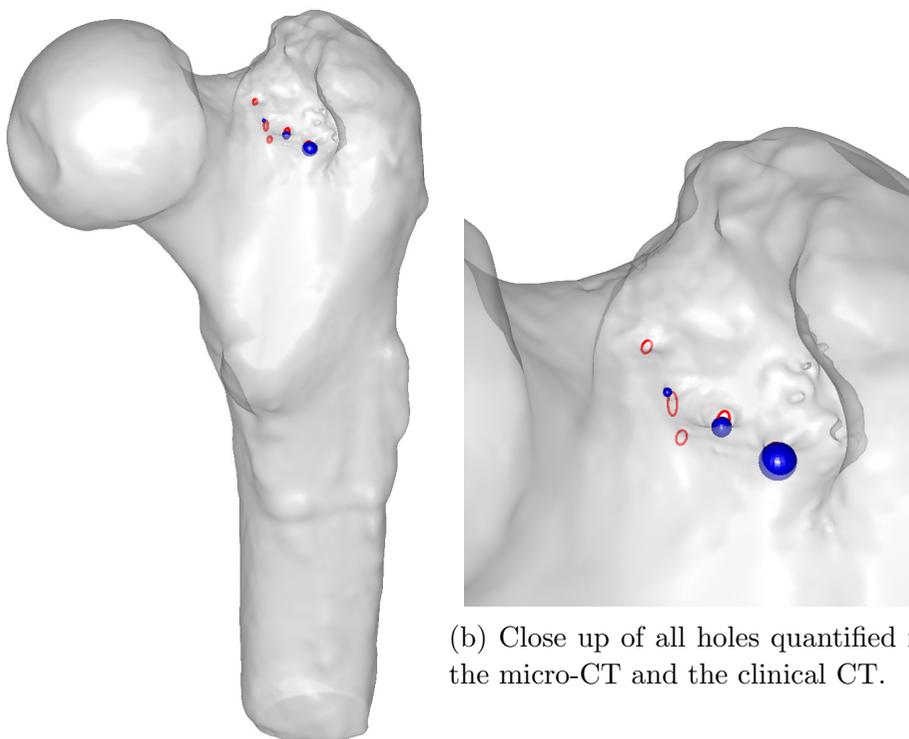
(b) Close up of all holes quantified in the micro-CT and the clinical CT.

(a) Femur with quantified vessel holes.

Figure 4.9: Quantified vessel holes in the final ROI in both the micro- and the clinical CT images, visualized together with the femur surface mesh. Red circles: micro-CT based quantified holes. Blue spheres: clinical CT based quantified holes.

4.2 Validation of the micro-FE model

In this section, the results for the validation of the micro-FE model will be presented. The validation will be divided into two parts: a qualitative comparison of the three FE models and comparison with experimental DIC data for the standard FE model and the micro-FE model.

4.2.1 Qualitative comparison

In the qualitative comparison, the predicted values for the minor principal strains were compared. First, the minor principal strains predicted by the reference model and the standard FE model were compared. Next, a comparison between the standard FE and micro-FE model was made. As a third step, the minor principal strains around detected vessel holes were compared between models. In all comparisons, the minor principal strains have negative values since the femoral neck is compressed. This means that when referring to higher minor principal strains, the interpretation should be that these strains are more negative and that the absolute value of the strains is higher.

Reference model and standard FE model

A comparison of the minor principal strains in the femur predicted by the reference model and the standard FE model shows that the magnitude of strains was similar (Figure 4.10). Both models predicted higher strains at the posterior lateral femoral neck than in the rest of the femur.

The predicted minor principal strains for the reference model and the standard FE model at the femoral neck (Figure 4.11) showed a similar pattern. However, the predicted strains in elements for the standard FE model seemed somewhat higher than for the reference model. Studying the femoral head, the strains were lower at the edge for the reference model, which could indicate a higher strength in the cortical bone for this model.
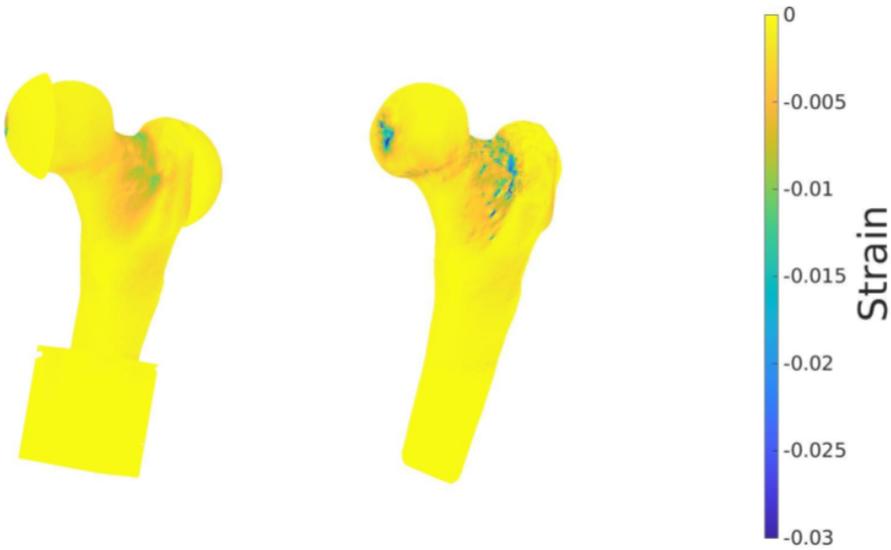
Figure 4.10: The predicted minor principal strains in the femur for the reference model (left) and the standard FE model (right), both showing higher predicted strains at the posterior lateral neck than in the rest of the femur.
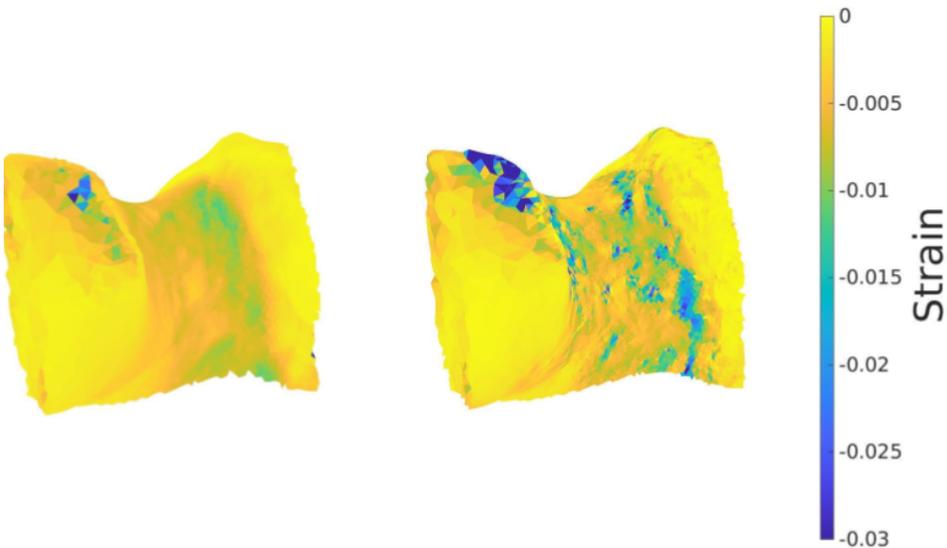
Figure 4.11: The predicted minor principal strains at the femoral neck for the reference model (left) and the standard FE model (right). The predicted strains showed a similar pattern, but the magnitude of predicted strains were slightly higher for the standard FE model.

Standard FE model and micro-FE model

A comparison of the minor principal strain, predicted by the standard
FE model and the micro-FE model (Figure 4.12) showed that the two
models were very similar in terms of predicted strain. Both show locally
higher minor principal strains at the posterior lateral femoral neck than
in the rest of the femur.
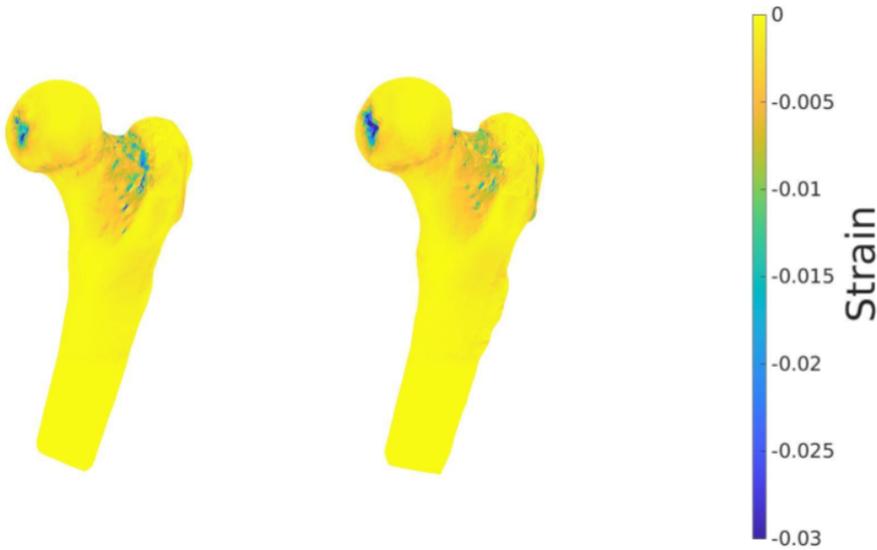
Figure 4.12: The predicted minor principal strains at the femoral neck
for the standard FE model (left) and the micro-FE model (right). Both
models predicted higher strains at the posterior lateral neck than in the
rest of the femur.

The minor principal strains predicted by the standard FE model and
the micro-FE model locally in the femoral neck (Figure 4.13) showed
that the magnitude of predicted strains was similar. Also, the strain
pattern was similar, but the distribution was different. For the standard
FE model, the high strains were covering large areas of the posterior side
of the lateral neck. Whereas, in the micro-FE, high strains were more
concentrated around smaller locations.
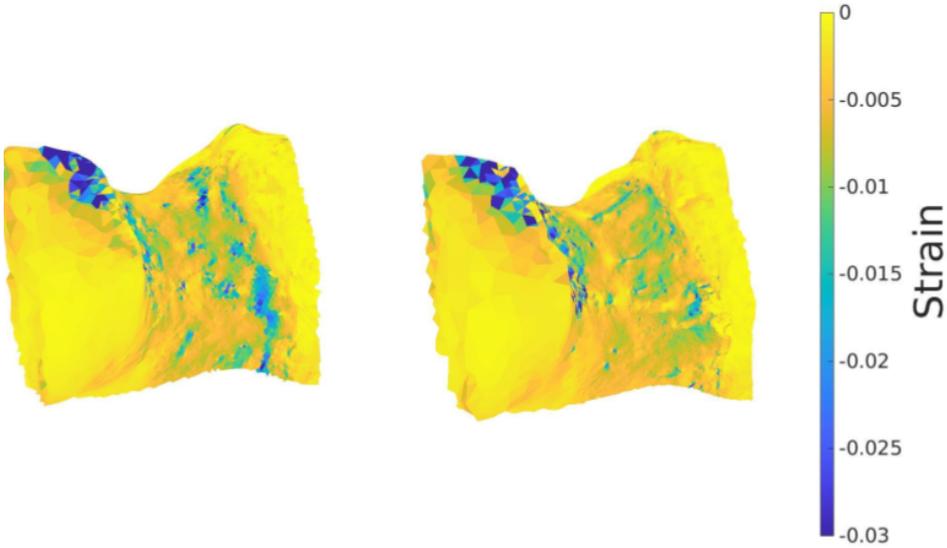
Figure 4.13: The predicted minor principal strains at the femoral neck for the standard FE model (left) and the micro-FE model (right). The predicted strains were similar in terms of magnitude, but the distribution was different.

Predicted strains in vessel holes

The minor principal strains around the vessel holes detected in micro-CT were investigated for the three FE models. The minor principal strains in external nodes around these positions were averaged (Table 4.5). What is interesting to note here is that the reference model predicted the lowest minor principal strain for all vessel holes, except for around vessel hole 1. Also noticeable is that the standard FE model predicted the highest (absolute) minor principal strain for all vessel holes.

Model	Hole 1	Hole 2	Hole 3	Hole 4	Hole 5
Reference	-0.0066	-0.0021	-0.0011	-0.0039	-0.0060
Standard FE	-0.0068	-0.0077	-0.0083	-0.0062	-0.0077
micro-FE	-0.0054	-0.0053	-0.0070	-0.0051	-0.0061

Table 4.5: The average predicted minor principal strain in external nodes surrounding the vessel holes for the three FE models.

The predicted minor principal strains were visualised for all models and all vessel holes quantified in micro-CT images. These figures are available in the Appendix. The predicted minor principal strains in elements around vessel holes 2 and 3 for the standard and micro-FE model (Figure 4.14) indicated that the standard FE model predicted slightly higher strains in external element, compared to corresponding positions in the micro-FE model.
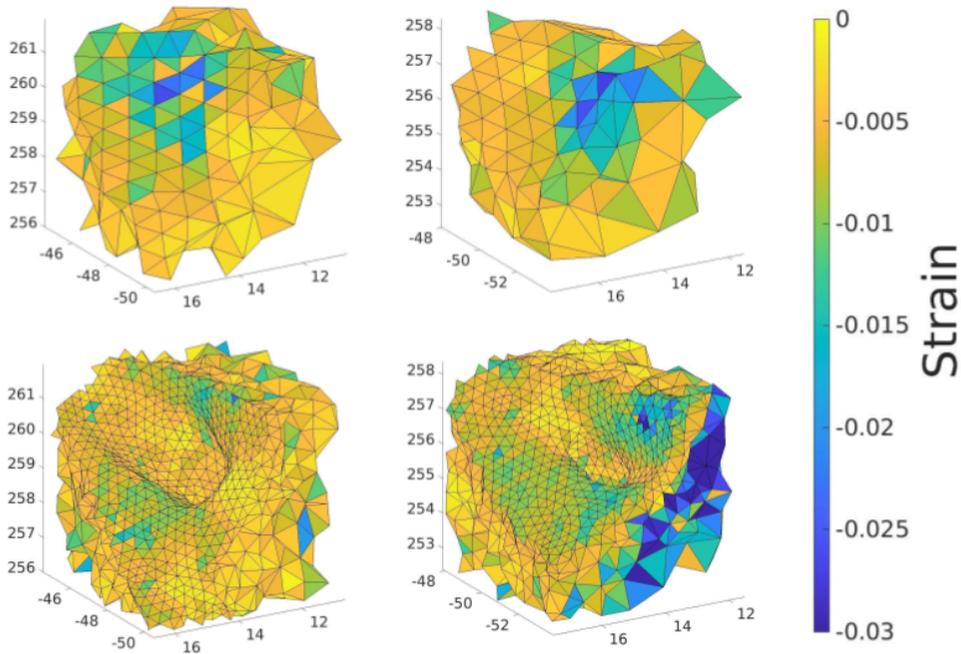
Figure 4.14: Visual comparison of predicted minor principal strains in a vessel hole 2 (left) and 3 (right) for the standard FE model (top) and the micro-FE model (bottom). In corresponding positions, the standard FE model seemed to predict slightly higher strains than the micro-FE model.

4.2.2 Validation with DIC

The external nodes of the standard FE model and the micro-FE model are shown, and the coloured nodes indicate which nodes of the FE models are included in the area where the DIC measurements were performed (Figure 4.15). When comparing the strains obtained experimentally to

the strains predicted by the FE models, the experimental strains were mapped onto the nodes indicated here.
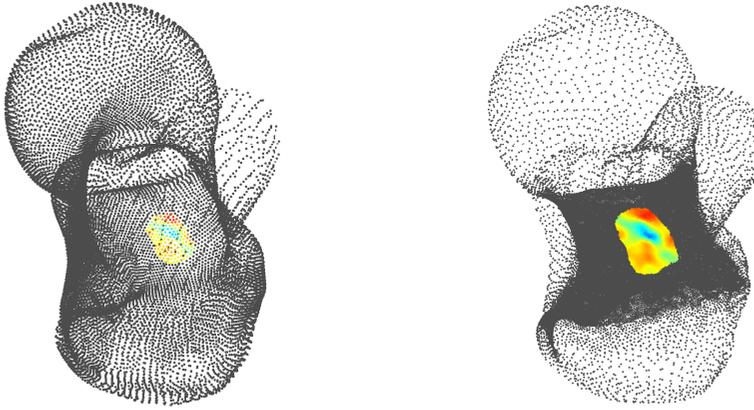
(a) Standard FE model.   (b) Micro-FE model.

Figure 4.15: External nodes of the standard FE model and the micro-FE model and experimentally measured strains mapped onto the meshes.

DIC for standard FE model

The area where DIC was performed is magnified (Figure 4.16) and the external nodes of the standard FE model within this area are shown. The predicted minor principal strain in external nodes and the experimental strains, mapped onto the same nodes, were compared and the difference in strain between the two measurements was determined. The experimentally measured strain detected a local weakness in the centre of the area. The predicted strain did not detect the same pattern, even though a few nodes in this area detected slightly higher strains. This indicated that there was no obvious correlation between measured and predicted strain for the standard FE model.

DIC for micro-FE model

The area where DIC was performed is magnified (Figure 4.17) for the micro-FE model. At first glance, the strains predicted and measured for the micro-FE model appear quite different, speaking for a low correlation between measured and predicted strain. Though, interesting to notice is that inside the area where the DIC detect the highest strains,

the micro-FE model showed a local weakness with a few nodes showing much higher strains than the surroundings.
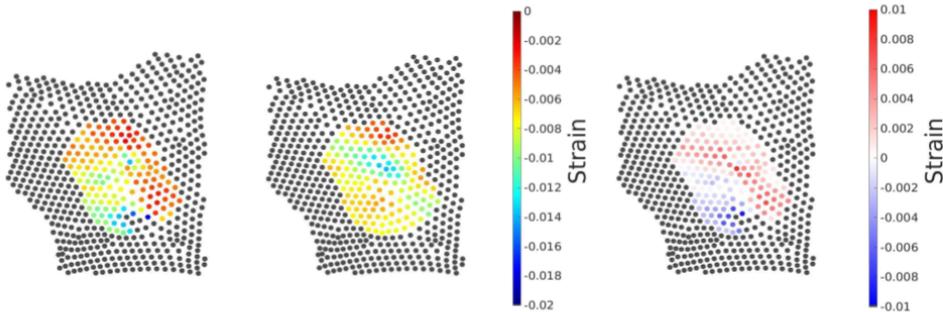
Figure 4.16: Predicted minor principal strains (left), experimental minor principal strains (center) and the difference between predicted and experimental strains (right) for external nodes of the standard FE model.
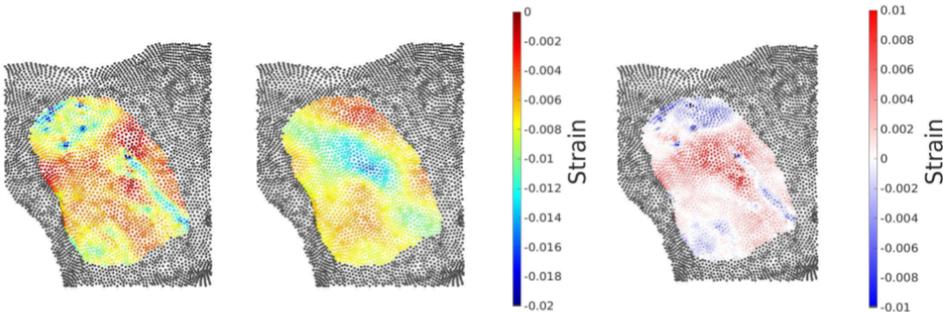
Figure 4.17: Predicted minor principal strains (left), experimental minor principal strains (center) and the difference between predicted and experimental strains (right) for external nodes of the micro-FE model.

Correlation and Bland-Altman plots

The strains predicted by FE models and the corresponding experimental strains can also be visualized as correlation, and Bland-Altman plots, as shown in Figure 4.18, where the correlation of both the major and minor principal strains is investigated. In the correlation plots, the parameter R^2 is closer to 1 for the micro-FE model indicating a better correlation between measured and predicted strain than the standard FE model. The stronger correlation for the micro-FE model was also indicated by

the confidence interval in the Bland-Altman plot, showing less difference between measurements for the micro-FE model.

(a) Standard FE, correlation plot.   (b) Standard FE, Bland-Altman plot.

(c) micro-FE, correlation plot.   (d) micro-FE, Bland-Altman plot.
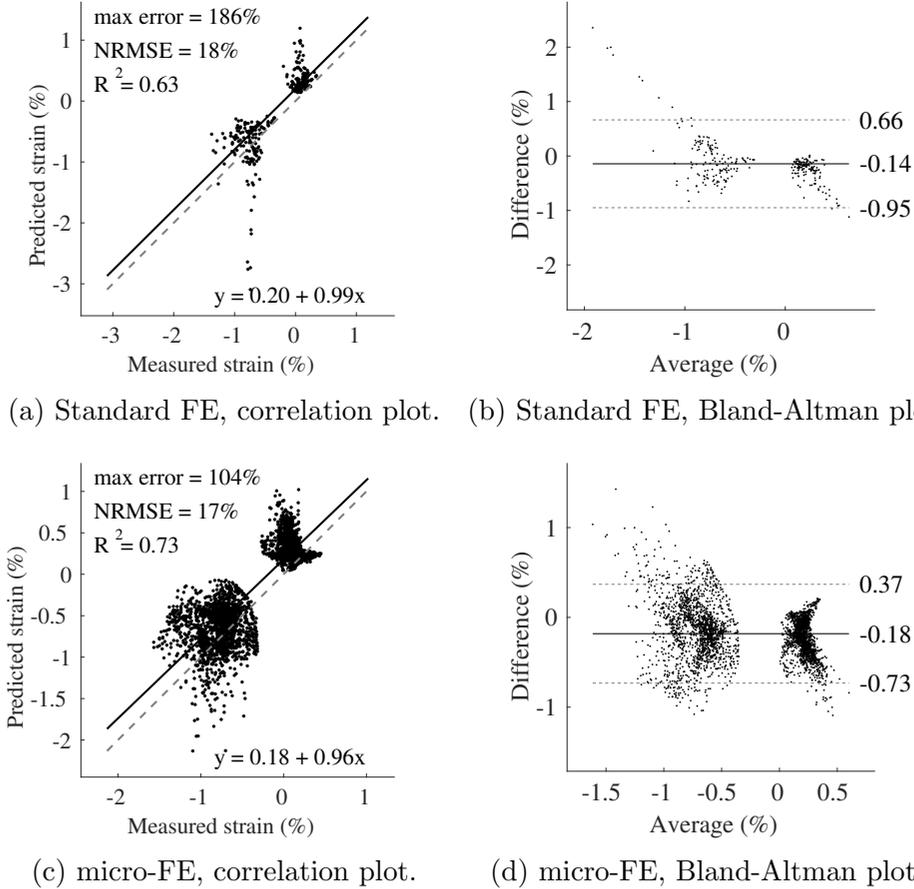
Figure 4.18: Correlation and Bland-Altman plots of the predicted and measured strains for the micro-FE model and the standard FE model. The correlation was stronger for the micro-FE model with a value of R^2 closer to 1, and less difference between measurements in the Bland-Altman plot.

Chapter 5

Discussion

This thesis aimed to investigate the effect of blood vessel holes on local strain distribution in the femoral neck, and determine the size and location of the holes.

Within this project, methods have been developed for detection and quantification of blood vessel holes from micro-CT images and clinical CT images. It was possible to generate a micro-FE model from segmentation of micro-CT images, partly based on full resolution micro-CT images. The micro-FE model predicted strains in the femoral neck better than a similar FE model based on clinical CT images.

5.1 Quantification of vessel holes

5.1.1 Micro-CT

The quantification of vessel hole in micro-CT images was developed to detect intersections, between a contour mesh of the ROI and shrunk surface meshes of the femur. The resulting intersections were fitted to circles representing the vessel holes. The method resulted in five well-described vessel holes detected totally automatic. All holes visible in the micro-CT image of the final ROI were detected and the size and location appeared correct. The only vessel hole showing tendency of misplacement is vessel hole 2 (Figure 4.5b), which was approximately 0.3 mm dislocated when comparing the result visually. But, with a total diameter of the hole of 2 mm, 0.3 mm was considered to be reasonable, and this small distance will probably not make a huge difference when implemented in FE models. Similarly, the radius in vessel hole 3 (Figure

4.5c), was underestimated by approximately 0.1 mm, but with the hole having a diameter of 2 mm, that was a small error.

The number of holes detected in the micro-CT images was in agreement with the literature in terms of size and location. Even though the distribution of vessel holes is very individual, studies reported an average of 4 ($\pm$1) holes in the superolateral part of the femoral neck close to the greater trochanter, and holes manually measured from less than 1 mm to larger than 2 mm in diameter in general [21, 22]. The quantified holes in the micro-CT ranged from 1.1 mm to 2 mm in diameter, which clearly is in the range of vessel holes measured in other studies.

However, the small errors described above, could be the result of the different intersection depths. The intersection depths represent the structure of the vessel hole canals, which have different shapes in the surface and throughout the cortical bone.

The selection of the ROI was crucial for the results obtained. The selection was based on previous research, as knowledge of the region where many vessel holes are present [21], and where high strain during a sideways fall is measured [13, 14], the choice aimed to identify the most interesting region, and best possible for this project. The final ROI was a region with well-defined vessel holes, optimal for proposing a method for quantification of vessel holes in the femoral neck in the human femur.

5.1.2   Clinical CT

The clinical CT method automatically detected vessel holes based on cortical bone thickness calculation. Based on a threshold value, the vessel holes were determined as very thin, or zero valued thickness regions. Thereafter, the vessel holes were quantified by size and location. Three vessel holes were detected by the clinical CT method, which were located accurately when compared to the micro-CT result. These three holes were the largest ones in the micro-CT, where they were quantified with a radius of approximately 1 mm. As the clinical CT imaged had a voxel size of 0.42 mm, it was not possible to detect objects much smaller than 1 mm. Thus, the detection of three holes shows great promise for future applicability of the proposed method.

The method was fairly sensitive to specific settings in the thickness calculation. Twelve parameter combinations were investigated in a full factorial scheme in order to identify the parameter set that resulted in

the highest accuracy, when compared to the reference micro-CT data. Since the clinical CT scans have a lower resolution it was not possible to identify vessel holes by eye, and the micro-CT data was chosen for the comparison of how accurate the method performed. The false positive detected holes were mostly found in the clinical CT scan reconstructed with a hard kernel together with the high-density mesh. This result could possibly be explained with the hard kernel images having sharp edges, resulting in the cortical thickness estimated thinner in more regions.

A threshold of the cortical bone thickness was set to classify a node as a hole (0.2 mm). A value was picked for the threshold, based on that the thickness of a hole should be zero, but with the possibility of a hole being estimated as a very thin region where a hole is present in the cortical bone. However, the sensitivity of variations in the results were investigated by varying the threshold from 0.1 - 0.5 mm. It was possible to show that the results were not very sensitive to the chosen threshold value, as threshold values of 0.1 - 0.3 mm showed a very similar result as the chosen one.

5.1.3 Evaluation

The micro-CT and clinical CT based approaches led to different results. The three vessel holes detected in the clinical CT images were overlapping with holes in the micro-CT result. The three holes detected with the clinical CT method corresponded with the three largest holes (approximate radii of 1 mm) detected with the micro-CT method. This could possibly be expected as the clinical CT images has lower resolution, thereby being more difficult to detect smaller holes.

The three overlapping holes in the two approaches were quantified differently by the clinical CT method. Comparing the clinical CT with the micro-CT as a reference, the clinical CT based approach both underestimated (41%) and overestimated (164%) the vessel hole size, indicating that the clinical CT method can detect the holes but cannot accurately determine their size (Table 5.1).

The clinical CT based approach detected 60% of the holes the micro-CT based method detects, where the smallest one detected in the clinical CT is of size 0.98 mm in radius according to micro-CT results. The largest one not detected in the clinical CT was of size 0.61 mm in radius according to the micro-CT. Notably, the clinical CT detected the largest

Scan	Radius [mm]		
Micro-CT	0.9843	0.9981	1.0015
Clinical CT	0.4044	0.8741	1.6376
% ($\frac{clin}{micro}$)	41%	88%	164%

Table 5.1: Two top rows: Radius of the overlapping quantified vessel holes from the micro-CT and clinical CT based methods. Bottom row: Percentage of the vessel hole radius in the clinical CT in relation to the micro-CT holes' radius.

holes, and likely those are the ones affecting the bone's properties the most. According to literature, many vessel holes in the femoral neck are < 1 mm in diameter [21]. No holes less than 1 mm were detected in the region of interest in this project, their effect on the predicted strain location and fractures in FE models will probably not be as large as the bigger holes.

5.2   Validation of the micro-FE model

The starting point for the FE modelling was the reference model that correlated well with experimental data in general, but not in areas surrounding vessel holes. For this reason, the project aimed to investigate whether a model with high resolution in the femoral neck could better represent the strains around vessel holes and correlate measured and predicted strains, even around vessel holes.

This was done by making a simplified FE model, and for validation, the standard FE model was created with a mesh density similar to the mesh density of the reference model. In this way, the modelling technique could be investigated, keeping the influence of the mesh basically constant. Later comparing the standard FE model to the micro-FE model would give an indication of how the importance of the mesh density in predicting strains in regions with vessel holes.

5.2.1 Qualitative comparison

Comparison of the standard FE model to the reference model showed that the predicted strains outside of the ROI were fairly similar (Figure 4.10). In the ROI, where the material mapping for the standard FE model was performed with micro-CT images, the minor principal strains were similar in terms of where at the femur the highest strains occurred, but the magnitude of the strains was slightly higher for the standard FE model (Figure 4.11). Overall, this indicated that the simplified standard FE model actually could be a good comparison to the validated reference model.

Evaluating the influence of a fine mesh, the standard FE model and the micro-FE model were compared, showing a very similar distribution in minor principal strain (Figure 4.12. Focusing on the superolateral femoral neck (Figure 4.13), it was interesting to notice that the magnitude of the strains appeared to be similar, but the distribution was different. In standard FE, the high strains were covering large areas of the posterior side of the lateral neck. Whereas, in the micro-FE, high strains were more concentrated around smaller locations. This observation was aligned with the results of minor principal strains in external nodes surrounding vessel holes (Table 4.5), where the standard FE model predicted higher average minor principal strain than the micro-FE model in all positions investigated.

The fact that the reference model predicts lower principal strains at the lateral neck could be explained by the fact that the model has a lower limit of its cortical bone strength, employed by having a minimum Young's modulus of 2.5 GPa in external elements. In this way, the influence of partial volume effects (PVE) is reduced. This could also explain that the reference model, in general, predicted the lowest value for principal strain around vessel holes (Table 4.5).

Interesting to discuss is why the predicted strains were different in the standard and micro FE model. One problem with the standard FE model was the fact that it was based on clinical CT images and, hence, has a rougher and less accurate geometry. This, together with the lower mesh density, is likely to give rise to partial volume effects during the mapping of the femur, causing a lower density of the cortical bone, which led to a weaker bone and higher predicted strains. Assuming the micro-FE model is better at predicting localized strains, this means that the areas of high strains in the standard FE model are over-predictions.

5.2.2   Validation with DIC

Due to the availability of DIC measurements, it was possible to perform quantitative validation of the strains predicted with the micro-FE and standard FE models.

The DIC measurements (Figure 4.18) showed that the measured strains correlated better with the strains predicted by the micro-FE model ($R^2 = 0.72$) than with the strains predicted by the standard FE model ($R^2 = 0.62$). This allows for saying that the micro-FE model in general was better at predicting strains than the standard FE model with lower mesh density.

The figures showing the strain measured with DIC (Figure 4.16 and 4.17) are detecting an area of local weakness in the centre of the DIC-area. This area has in a previous study been correlated with a vessel hole [14]. The same clear pattern cannot be seen in the corresponding figures of predicted strains. Studying the strains predicted by the micro-FE model, the high strains appeared to be local rather than distributed over a larger surface. One explanation for this could be that the strains predicted by the micro-FE models were not that accurate and that the local high strains were caused by occasional elements with low density at the surface. It could also be that the absence of high strains in the micro-FE model surrounding the vessel holes is an indication that the high strains measured by DIC were not caused by deformation of the bone itself. Other underlying causes for these strains could be the remaining presence of soft tissue, or fluids leaking out of the hole deforming the paint.

Previous studies suggested that introducing vessel holes in FE models could improve the prediction of strains [13] [12]. Based on the current results the results, this cannot be validated. However, the finding that the strains predicted by a micro-FE model correlated better than a similar model based on clinical CT images to experimentally measured strains is an indication that the mesh density is relevant and that this is something to further look into.

Worth mentioning when discussing the results of the DIC measurements is that the number of comparisons was very different for the standard FE model and the micro-FE model. The standard FE model had more distinguished outliers than the micro-FE model, which in combination with the lower number of comparisons could be the reason for the correlation to be worse for the standard FE model.

5.3 Future perspective

The project successfully developed methods for detecting and quantifying blood vessel holes, both in micro-CT images and in clinical CT images. Today, it is possible to generate a micro-FE model, from a segmentation of micro-CT images, partly based on full resolution micro-CT images. The micro-FE model predicted strains in the femoral neck better than a similar FE model based on clinical CT images when compared to experimentally measured strains.

The material used in this project was limited to only one femur. Even if automatic methods were developed and applied to this femur, a further investigation, in terms of applying the method on several femurs, is still required. The most immediate future evolution for this project would be to evaluate the same methodology over multiple femoral anatomies. Then, it would be possible to see the effects of the blood vessel holes in the FE models on a larger scale, and investigate whether FE models of other femurs will predict similar strains in vessel hole regions as the micro-CT based models in this project did. How the strain prediction in FE modeling is affected by implementation of vessel holes considering an overall perspective, of many femurs investigated, would be something that could possibly conclude the impact of vessel holes on another level of certainty, and is a question for future studies to address.

Due to computational resources, it was not possible to build FE models completely based on full-resolution micro-CT images, consisting of many fine elements in the whole surface mesh. A more powerful computer could potentially address this limitation, and overcome the issue. It would be interesting to continue this work, looking into how a FE-model completely based on full-resolution micro-CT images would perform. How implementation of vessel holes in a bigger area would affect the predicted strains, if that would increase the model performance even more, or if the FE model partly based on full resolution micro-CT images is good enough. However, with the prospect of developing FE models clinically, it is not an alternative with micro-CT images. Therefore, developing models partly based of micro-CT images is a more realistic way of proceeding. This is, as mentioned, something for future studies to address.

This project contributed to further research by the development of a framework with which a micro-FE model can be generated including

a complex surface structure. This can be a foundation for a new way of estimations of fracture risk in patients clinically. By further improvement of the method for detecting and quantifying vessel holes in clinical CT images and including these in micro-FE models, the continuation is exciting to follow. The method could be the starting point for future possibilities of large scale screening of patients for high fracture risk, even in people without osteoporosis.

5.4   Ethical aspects

The CT scans used in this project were already collected in another study, and ethically approved for use (by The Finnish National Authority for Medicolegal Affairs, TEO, 5783/04/044/07) [14]. No new samples were collected for this study.

The methods are today not ready for clinical implementation. Maybe a patient's need of knowing about the distribution of vessel holes in the femoral neck is not a strong argument for such an implementation. However, if the method could improve fracture risk assessments, it could in the bigger picture be something valuable even for the patient as an individual. It could contribute to improved quality of life in a patient belonging to a risk group.

The methods in the project required CT images of human femurs, something that should be considered from an ethical aspect if the methods would be further investigated with new CT scans or, implemented clinically in the future. The amount of radiation is constrained and always aimed to be minimized in an individual. If one would re-use already existing CT scans during the development of the method, the screening will be reduced. Considering a clinical implementation when screening will be necessary, if reducing the screening to people in risk groups or with certain diseases, the gain of the screening could possibly be greater than the risks. If it is possible to in an early stage diagnose and find patients at risk for fragility fractures, or having a bone disease, treatments could be given to more patients. This could lead to decreased costs and improved quality of life in individuals, and possibly could the risk of fracture be reduced, or maybe even eliminated.

Chapter 6

Conclusions

The conclusion is that vessel holes can automatically be detected and quantified fully from micro-CT images and partly from clinical CT images. A micro-FE model generated based on micro-CT images, including the vessel holes in the femoral neck, correlated better than a similar model based on clinical CT images to experimentally measured strains.

The micro-CT based approach could accurately quantify the vessel holes, while the clinical CT based approach quantified 60% of the holes found in the micro-CT, the largest holes in terms of radius size.

A micro-FE model was developed from micro-CT images including the vessel holes in the geometry of the femur. The model showed higher accuracy in strain prediction than a similar FE model based on clinical CT images. The results indicated that including vessel holes in FE models could have an influence on the prediction of strains at the superolateral femoral neck, and should be accounted for in future FE models.

Bibliography

[1] International Osteoporosis Foundation. What is Osteoporosis?, 2017. `http://iofbonehealth.org/what-is-osteoporosis`. [Online; accessed 2020-02-28].

[2] Fredrik Borgström, Linda Karlsson, Gustav Ortsäter, Nicolas Norton, Philippe Halbout, Cyrus Cooper, Mattias Lorentzon, Eugene V. McCloskey, Nicholas C. Harvey, Muhamamd K. Javaid, John A. Kanis, and International Osteoporosis Foundation. Fragility fractures in Europe: burden, management and opportunities. *Archives of Osteoporosis*, 15(1):59, 2020.

[3] J. A. Kanis, A. Odén, E. V. McCloskey, H. Johansson, D. A. Wahl, C. Cooper, and on behalf of the IOF Working Group on Epidemiology and Quality of Life. A systematic review of hip fracture incidence and probability of fracture worldwide. *Osteoporosis International*, 23(9):2239–2256, September 2012.

[4] Axel Svedbom, Emma Hernlund, Moa Ivergard, Juliet Compston, Cyrus Cooper, Judy Stenmark, Eugene Mccloskey, Bengt Jonsson, George Lyritis, Polyzois Makras, and John Kanis. Epidemiology and Economic Burden of Osteoporosis in Greece. *Archives of Osteoporosis*, 8:83–90, October 2013.

[5] B. Gullberg, O. Johnell, and J. A. Kanis. World-wide projections for hip fracture. *Osteoporosis international: a journal established as result of cooperation between the European Foundation for Osteoporosis and the National Osteoporosis Foundation of the USA*, 7(5):407–413, 1997.

[6] John A Kanis. Diagnosis of osteoporosis and assessment of fracture risk. *The Lancet*, 359(9321):1929–1936, June 2002.

[7] John A. Kanis, Frederik Borgstrom, Chris De Laet, Helena Johansson, Olof Johnell, Bengt Jonsson, Anders Oden, Niklas Zethraeus, Bruce Pfleger, and Nikolai Khaltaev. Assessment of fracture risk. *Osteoporosis International*, 16(6):581–589, June 2005.

[8] International Osteoporosis Foundation. Diagnosing Osteoporosis, 2017. `https://www.iofbonehealth.org/diagnosing-osteoporosis`. [Online; accessed 2020-03-05].

[9] Ethel S. Siris, Ya-Ting Chen, Thomas A. Abbott, Elizabeth Barrett-Connor, Paul D. Miller, Lois E. Wehren, and Marc L. Berger. Bone Mineral Density Thresholds for Pharmacological Intervention to Prevent Fractures. *Archives of Internal Medicine*, 164(10):1108–1112, May 2004. Publisher: American Medical Association.

[10] Lorenzo Grassi, Sami P. Väänänen, Matti Ristinmaa, Jukka S. Jurvelin, and Hanna Isaksson. How accurately can subject-specific finite element models predict strains and strength of human femora? Investigation using full-field measurements. *Journal of Biomechanics*, 49(5):802–806, March 2016.

[11] B. Helgason, S.Gilchrist, O. Ariza, J. D. Chak, G. Zheng, R. P. Widmer, S. J. Ferguson, P. Guy, and P. A. Cripton. Development of a balanced experimental–computational approach to understanding the mechanics of proximal femur fractures. *Medical Engineering & Physics*, 36(6):793–799, June 2014.

[12] Hassan Bahaloo, W. S. Enns-Bray, I. Fleps, O. Ariza, S. Gilchrist, R. Widmer Soyka, P. Guy, H. Palsson, S. J. Ferguson, P. A. Cripton, and B. Helgason. On the Failure Initiation in the Proximal Human Femur Under Simulated Sideways Fall. *Annals of Biomedical Engineering*, 46(2):270–283, February 2018.

[13] Yekutiel Katz and Zohar Yosibash. New insights on the proximal femur biomechanics using Digital Image Correlation. *Journal of Biomechanics*, 101:109599, March 2020.

[14] Lorenzo Grassi, Joeri Kok, Anna Gustafsson, Yi Zheng, Sami P. Väänänen, Jukka S. Jurvelin, and Hanna Isaksson. Elucidating

failure mechanisms in human femurs during a fall to the side using bilateral digital image correlation. *Journal of Biomechanics*, 106:109826, June 2020.

[15] Lumen Learning. Anatomical Orientation and Directions | Human Anatomy and Physiology Lab (BSB 141). `https://courses.lumenlearning.com/ap1x94x1/chapter/anatomical-orientation-and-directions/`. [Online; accessed 2020-05-20].

[16] Paul Jackson Mansfield and Donald A. Neumann. Chapter 9 - Structure and Function of the Hip. In Paul Jackson Mansfield and Donald A. Neumann, editors, *Essentials of Kinesiology for the Physical Therapist Assistant (Third Edition)*, pages 233–277. Mosby, St. Louis (MO), January 2019.

[17] Fêmur - Anatomia do maior osso do corpo humano. Library Catalog: `www.anatomiaemfoco.com.br`. [Online; accessed 2020-05-20].

[18] U. F. O. Themes. PELVIS AND UPPER FEMORA, March 2016. Library Catalog: `https://radiologykey.com/pelvis-and-upper-femora/`. [Online; accessed 2020-05-20].

[19] Bone - Bone morphology. Library Catalog: `www.britannica.com`. [Online; accessed 2020-06-02].

[20] Kunio Ishikawa. Bone Substitute Fabrication Based on Dissolution-Precipitation Reactions. *Materials*, 3(2):1138–1155, February 2010.

[21] Jiong Mei, Ming Ni, Guoliang Wang, Guangyao Jia, Shiwei Liu, Xueliang Cui, Chao Jiang, Hua Wang, Yahui Dai, Kun Quan, and Rui Chen. Number and distribution of nutrient foramina within the femoral neck and their relationship to the retinacula of Weitbrecht: an anatomical study. *Anatomical Science International*, 92(1):91–97, 2017.

[22] Martin Lavigne, Morteza Kalhor, Martin Beck, Reinhold Ganz, and Michael Leunig. Distribution of Vascular Foramina Around the Femoral Head and Neck Junction: Relevance for Conservative Intracapsular Procedures of the Hip. *Orthopedic Clinics of North America*, 36(2):171–176, April 2005.

[23] U.S. Department of Health & Human Services Na-
     tional Institute of Biomedical Imaging and Bioengineer-
     ing (NIBIB). Computed Tomography (CT). `https:
     //www.nibib.nih.gov/science-education/science-topics/
     computed-tomography-ct`. [Online; accessed 2020-03-13].

[24] Micro Photonics Inc. What is Micro-CT? An Introduc-
     tion, February 2018. `https://www.microphotonics.com/
     what-is-micro-ct-an-introduction/`. [Online; accessed 2020-
     03-13].

[25] Euclid Seeram. *Computed Tomography - E-Book: Physical Prin-
     ciples, Clinical Applications, and Quality Control*. Elsevier Health
     Sciences, September 2015. Google-Books-ID: DTCDCgAAQBAJ.

[26] Nick McCormick and Jerry Lord. Digital Image Correlation. *Ma-
     terials Today*, 13(12):52–54, December 2010.

[27] Bing Pan, Zhaoyang Wang, and Zixing Lu. Genuine full-field
     deformation measurement of an object with complex shape us-
     ing reliability-guided digital image correlation. *Optics Express*,
     18(2):1011–1023, January 2010. Publisher: Optical Society of
     America.

[28] Lorenzo Grassi. *Femoral Strength Prediction using Finite Element
     Models : Validation of models based on CT and reconstructed DXA
     images against full-field strain measurements*. thesis/doccomp,
     Lund University, 2016. ISBN: 9789177530312 9789177530305.

[29] Nurettin Özgür Doğan. Bland-Altman analysis: A paradigm to un-
     derstand correlation and agreement. *Turkish Journal of Emergency
     Medicine*, 18(4):139–141, December 2018.

[30] Coefficient of determination | Interpretation & Equation. Library
     Catalog: `www.britannica.com`. [Online; accessed 2020-06-06].

[31] Bland–Altman plot, May 2020. `https://en.wikipedia.org/
     wiki/Bland-Altman_plot`. [Online; accessed 2020-06-04].

[32] Chiranji Lal Chowdhary and D. P. Acharjya. Segmentation and
     Feature Extraction in Medical Imaging: A Systematic Review. *Pro-
     cedia Computer Science*, 167:26–36, January 2020.

[33] Paul A. Yushkevich, Joseph Piven, Heather Cody Hazlett, Rachel Gimpel Smith, Sean Ho, James C. Gee, and Guido Gerig. User-guided 3D active contour segmentation of anatomical structures: Significantly improved efficiency and reliability. *NeuroImage*, 31(3):1116–1128, July 2006.

[34] Vicent Caselles, Francine Catté, Tomeu Coll, and Françoise Dibos. A geometric model for active contours in image processing. *Numerische Mathematik*, 66(1):1–31, December 1993.

[35] V. Caselles, R. Kimmel, and G. Sapiro. Geodesic active contours. In *Proceedings of IEEE International Conference on Computer Vision*, pages 694–699, Cambridge, MA, USA, 1995. IEEE Comput. Soc. Press.

[36] Machine Intelligence Laboratory Cambridge University Department of Engineering. Stradview 6.0, 2014. `https://mi.eng.cam.ac.uk/Main/StradView`. [Online; accessed 2020-05-20].

[37] G. M. Treece and A. H. Gee. Independent measurement of femoral cortical thickness and cortical bone density using clinical CT. *Medical Image Analysis*, 20(1):249–264, February 2015.

[38] G. M. Treece, A. H. Gee, P. M. Mayhew, and K. E. S. Poole. High resolution cortical bone thickness measurement from clinical CT data. *Medical Image Analysis*, 14(3):276–290, June 2010.

[39] R. K. Nalla, J. H. Kinney, and R. O. Ritchie. Mechanistic fracture criteria for the failure of human cortical bone. *Nature Materials*, 2(3):164–168, March 2003.

[40] Elise F Morgan and Tony M Keaveny. Dependence of yield strain of human trabecular bone on anatomic site. *Journal of Biomechanics*, 34(5):569–577, May 2001.

[41] Niels Saabye Ottosen and Hans Petersson. *Introduction to the finite element method*. Prentice Hall, New York, 1992.

[42] Element Types. `http://web.mit.edu/calculix\_v2.7/CalculiX/ccx\_2.7/doc/ccx/node25.html`. [Online; accessed 2020-05-24].

[43] Fulvia Taddei, Enrico Schileo, Benedikt Helgason, Luca Cristofolini, and Marco Viceconti. The material mapping strategy influences the accuracy of CT-based finite element models of bones: An evaluation against experimental measurements. *Medical Engineering & Physics*, 29(9):973–979, November 2007.

[44] Enrico Schileo, Fulvia Taddei, Luca Cristofolini, and Marco Viceconti. Subject-specific finite element models implementing a maximum principal strain criterion are able to estimate failure risk and fracture location on human femurs tested in vitro. *Journal of Biomechanics*, 41(2):356–367, January 2008.

[45] Elise F. Morgan, Harun H. Bayraktar, and Tony M. Keaveny. Trabecular bone modulus–density relationships depend on anatomic site. *Journal of Biomechanics*, 36(7):897–904, July 2003.

[46] Scientific Computing and Imaging Institute. Seg3D 2.4.4, 2016. `http://www.sci.utah.edu/cibc-software/seg3d.html`. [Online; accessed 2020-04-17].

[47] Autodesk Inc. Meshmixer 3.5. `http://www.meshmixer.com/`. [Online; accessed 2020-04-17].

[48] Qianqian Fang and David A. Boas. Tetrahedral mesh generation from volumetric binary and grayscale images. In *2009 IEEE International Symposium on Biomedical Imaging: From Nano to Macro*, pages 1142–1145, Boston, MA, USA, June 2009. IEEE.

[49] Jaroslaw Tuszynski. Surface intersection, May 2020. `https://se.mathworks.com/matlabcentral/fileexchange/48613-surface-intersection`. [Online; accessed 2020-06-14].

[50] Jaroslaw Tuszynski. Triangle/Ray Intersection, May 2020. `https://se.mathworks.com/matlabcentral/fileexchange/33073-triangle-ray-intersection`. [Online; accessed 2020-05-14].

[51] Sam Murthy. Best fit 3D circle to a set of points, May 2020. `https://se.mathworks.com/matlabcentral/fileexchange/55304-best-fit-3d-circle-to-a-set-of-points`. [Online; accessed 2020-05-14].

[52] Enrico Schileo, Jonathan Pitocchi, Cristina Falcinelli, and Fulvia Taddei. Cortical bone mapping improves finite element strain prediction accuracy at the proximal femur. *Bone*, 136:115348, July 2020.

[53] Peter Karasev. Triangle subdivide (vectorized/fast), May 2020. `https://se.mathworks.com/matlabcentral/fileexchange/25961-triangle-subdivide-vectorized-fast`. [Online; accessed 2020-05-14].

[54] Dr Michael D Abràmoff. Image Processing with ImageJ. *Biophotonics International, Laurin Publishing Co. Inc*, July 2004.

[55] Hyperworks 2019 | Solutions for Every Stage of Product Development. `https://www.altair.com/hyperworks-2019/`. [Online; accessed 2020-05-26].

[56] Abaqus Unified FEA - SIMULIA™ by Dassault Systèmes®. Library Catalog: `www.3ds.com`. [Online; accessed 2020-05-26].

[57] CloudCompare - Open Source project. `https://www.cloudcompare.org/`. [Online; accessed 2020-04-17].

Appendix

## 7.1 Strain in vessel holes

Reference model
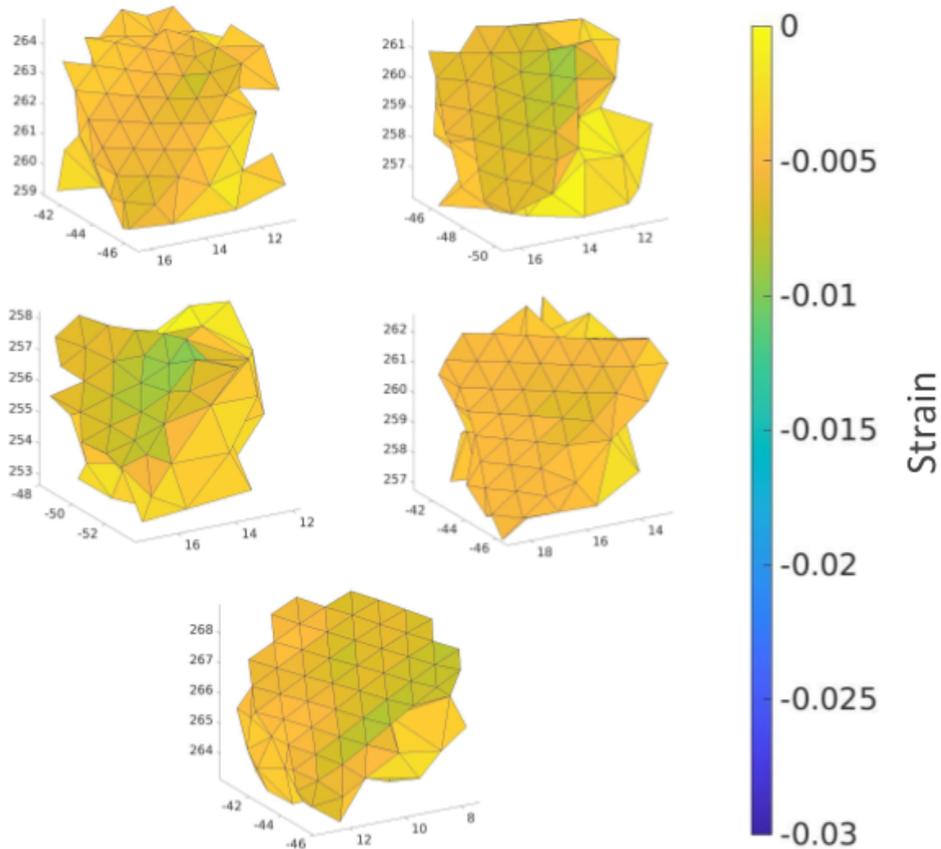
Figure 7.1: Predicted strain in detected vessel hole 1 (top left) to 5 (bottom) for the reference model.

Standard FE model
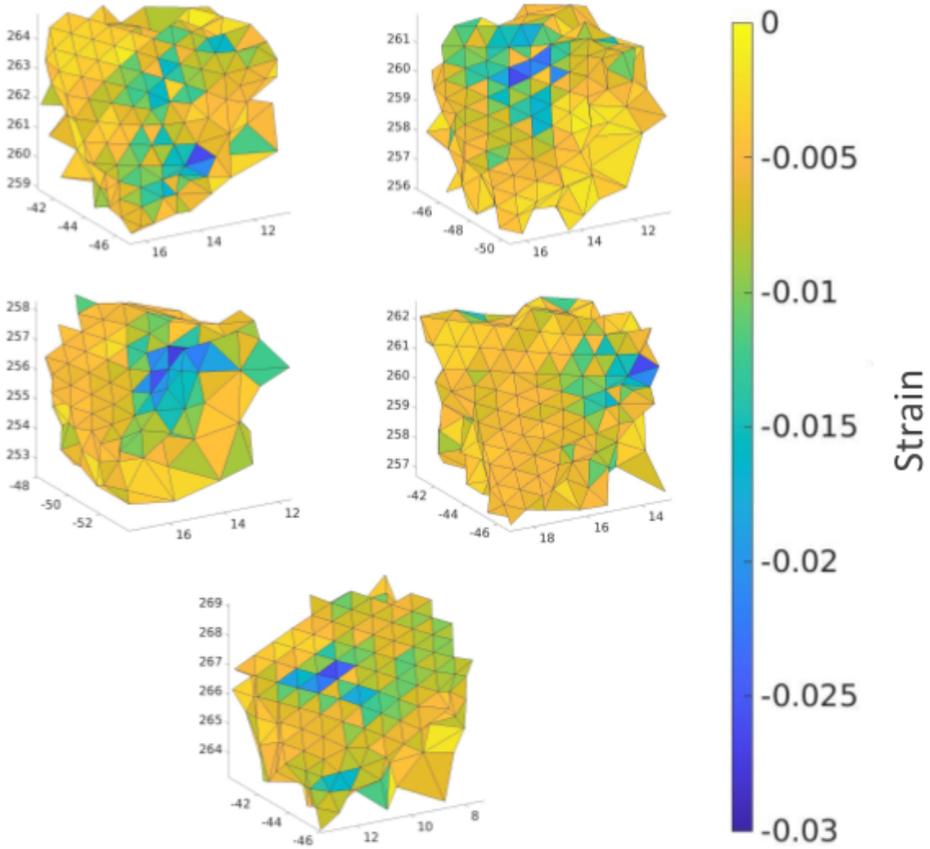
Figure 7.2: Predicted strain in detected vessel hole 1 (top left) to 5 (bottom) for the standard model.

Micro-FE model
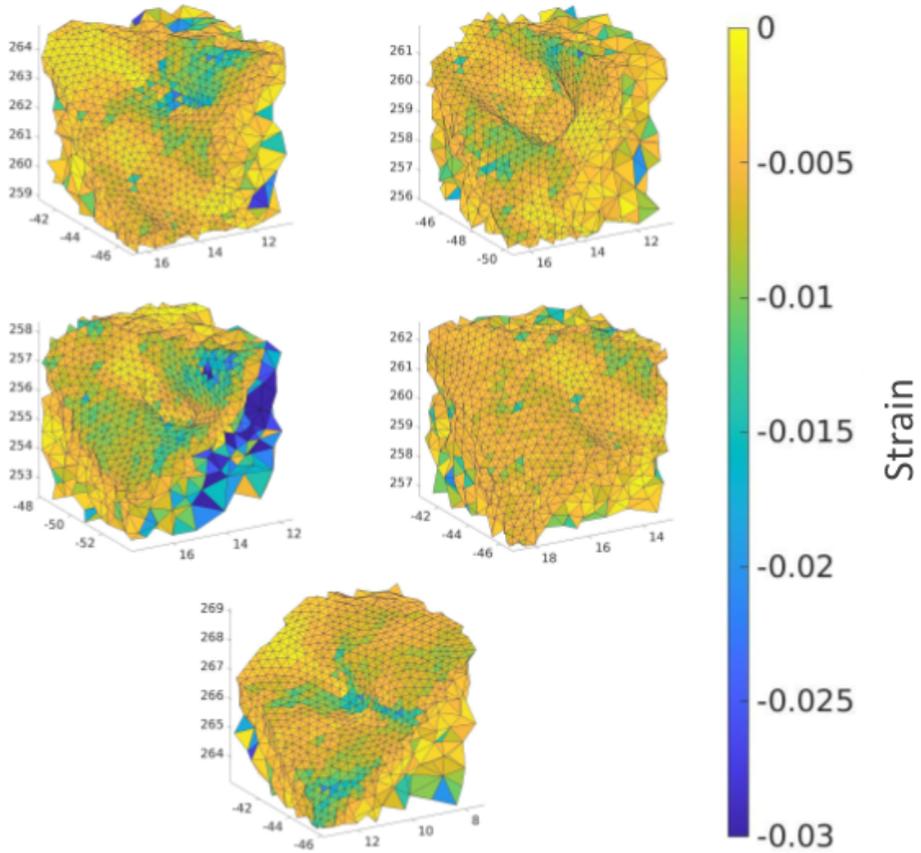
Figure 7.3: Predicted strain in detected vessel hole 1 (top left) to 5 (bottom) for the micro-FE model.